

¹ Physics-Infused Reduced-Order Modeling for Analysis of
² Ablating Hypersonic Thermal Protection Systems

³

⁴ November 26, 2025

⁵

Abstract

This work presents a *physics-infused reduced-order modeling* (PIROM) framework towards design, analysis, and optimization of non-decomposing ablating hypersonic thermal protection systems (TPS), and is demonstrated via the modeling of transient thermo-ablative responses of multi-layered hypersonic TPS. The PIROM architecture integrates a reduced-physics backbone, based on the lumped-capacitance model (LCM) and a surface recession model (SRM), with data-driven correction dynamics formulated via a coarse-graining approach rooted in the Mori-Zwanzig formalism. The LCM is coupled to the SRM to capture the one-dimensional surface recession of the ablating TPS as a function of the surface temperature. While the LCM and SRM capture the dominant physics of the ablating TPS response, the correction terms compensate for residual dynamics arising from higher-order non-linear interactions and temperature-advection effects due to surface recession. The PIROM consistently achieves errors of $\approx 0.5\%$ for a wide range of extrapolative settings of design parameters involving time-and-space varying boundary conditions and SRM models, and improves by an order of magnitude by the LCM alone. Moreover, the PIROM delivers online evaluations that are two orders of magnitude faster than the full-order model (FOM). These results demonstrate that PIROM effectively reconciles the trade-offs between accuracy, generalizability, and efficiency, providing a promising framework for optimizing multi-physical dynamical systems, such as TPS, under diverse operating conditions.

²⁵

1 Introduction

²⁶ At hypersonic speeds, aerospace vehicles experience extreme aero-thermo-dynamic environments that require specialized thermal protection systems (TPS) to shield internal sub-²⁷ structures, electronics, and possibly crew members from the intense aerodynamic heating.²⁸ The TPS is composed of ablating materials to withstand the high-energy physics – a high-²⁹ temperature capable fibrous material injected with a resin that fills the pore network and³⁰ strengthens the composite [1]. The TPS design promotes the exchange of mass through³¹ thermal and chemical reactions (i.e., ablation), effectively mitigating heat transfer to the³² sub-structures. As a result, accurate prediction for the ablating TPS response under ex-³³ treme hypersonic heating becomes critical to ensuring survivability, performance, and safety³⁴ of hypersonic vehicles. Not only is it necessary to assess the performance of the thermal³⁵

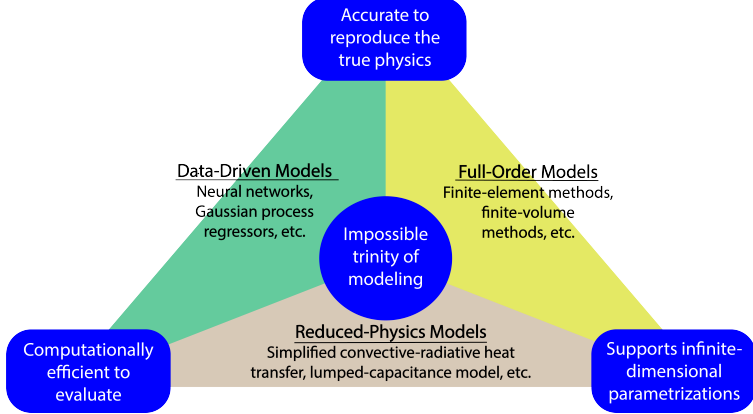


Figure 1: The impossible trinity of modeling: accuracy, generalizability, and efficiency.

management systems, but also the shape changes of the vehicle’s outer surface induced by the ablating material, and its impact on the aerodynamics, structural integrity, and controllability.

Even with today’s advancements in computational resources and numerical methods, high-fidelity simulations of ablating TPS remains a formidable challenge, both theoretically and computationally. On the theoretical side, the thermo-chemical reactions, coupled with the irregular pore network structure and ablating boundaries, translate into complex non-linear equations governing multi-physical interactions across several spatio-temporal scales [1, 8]. On the computational side, numerical approaches based on finite-element (FEM) or finite-volume (FVM) methods yield systems of differential equations modeling the transient thermo-ablative response of the TPS [5]. The FEM discretizations lead to high-dimensional systems of equations, resulting in prohibitive computational costs for many-query applications such as design, optimization, uncertainty quantification, and real-time applications, where possibly thousands of model evaluations are required.

Reduced-order models (ROMs) have emerged as a promising approach to alleviate the computational costs of high-fidelity simulations [6, 11]. Ideally, a ROM should be: (1) accurate to reproduce high-fidelity solutions, (2) support continuous or infinite-dimensional design parameters such as geometrical shapes and material distributions, (3) be computationally efficient to evaluate to allow for fast turnaround times in design optimization. However, the above three capabilities usually form an *impossible trinity of modeling*, as illustrated in Fig. 1; building a ROM that achieves any two capabilities sacrifices the third.

The impossible trinity poses a significant challenge in the development of ROMs for the multi-disciplinary transient analysis and optimization of ablating TPS. Specifically, full-order models (FOMs), e.g., FEMs or FVMs, offer high accuracy and robust generalization over design spaces, but are computationally expensive to evaluate. Reduced-physics models (RPMs) – such as simplified convective-radiative heat transfer or engineering correlations – are low-dimensional models that achieve efficiency and broad applicability by ignoring higher-order non-linear effects. However, RPMs sacrifice accuracy for complex thermo-ablative responses due to the simplifications and assumptions inherent in their formulation, and it is generally not clear how to systematically leverage existing high-fidelity data to improve RPMs [18].

67 Lastly, data-driven ROMs, such as Gaussian Process Regression (GPR) [?], Neural Net-
68 works (NNs), and neural ordinary differential equations (NODEs) [3], can provide accurate
69 and computationally-efficient approximations of high-fidelity models for complex thermo-
70 ablative responses. However, these data-centric approaches often demand extensive high-
71 fidelity data for training, do not necessarily satisfy fundamental physical constraints or con-
72 servation laws, and thus do not generalize well to the design spaces outside the training [16].

73 This work presents the extension of the *physics-infused reduced-order modeling* (PIROM)
74 framework to include effects of ablation for TPS applications, previously ignored in Ref. [17].
75 Specifically, the PIROM is demonstrated for the transient thermo-ablative response of multi-
76 layered hypersonic TPS. The PIROM is a non-intrusive framework that combines the strengths
77 of physics-based models with machine learning to formulate and train ROMs for parametrized
78 non-linear dynamical systems. The backbone of the PIROM is the physics-based component,
79 i.e., the RPM, which in this work is composed of: (1) a *lumped capacitance model* (LCM)
80 to model the average heat transfer within the TPS layers, and (2) a *surface recession model*
81 (SRM) to model one-dimensional surface ablation.

82 Leveraging the *Mori-Zwanzig* (MZ) formalism [15, 14, 13], the RPM is rigorously ex-
83 tended with data-driven hidden dynamics to account for the missing physics in the LCM,
84 which are learned from high-fidelity data. The hidden dynamics enable higher predictive
85 accuracy of the PIROM when subjected to complex boundary conditions and SRM model
86 variations. For the TPS problem, the MZ approach produces a sufficiently simple model
87 form while maintaining the physical consistency of the PIROM, as well as the dependence
88 on design parameters. Thus, the PIROM aims to solve the ITM by leveraging the gen-
89 eralizability and computational efficiency of RPMs, while incorporating the accuracy and
90 adaptability of data-driven extensions. More importantly, the PIROM formulation provides
91 a general methodology for developing PIROMs for other multi-physics problems.

92 The specific objectives of this work are summarized as follows:

- 93 1. Extend the previous PIROM formulation in Ref. [17] to model transient thermo-
94 ablative response of multi-layered hypersonic TPS through a systematic coarse-graining
95 procedure based on the Mori-Zwanzig formalism.
- 96 2. Benchmark the accuracy, generalizability, and computational accelerations of the PIROM
97 against the RPM and the high-fidelity FEM solutions of ablating TPS, thus quanti-
98 fying the PIROM’s capabilities to solve the ITM in complex multi-physical non-linear
99 dynamical systems.

100 2 Modeling of Thermal Protection Systems

101 This section presents the problem of modeling the transient thermo-ablative response of a
102 non-decomposing TPS, subjected to extreme hypersonic heating. Two different but math-
103 ematically connected solution strategies are provided: (1) a high-fidelity full-order model
104 (FOM) based on a finite element method (FEM), and (2) a RPM based on a *lumped ca-*
105 *pacitance model* (LCM) and a one-dimensional *surface recession model* (SRM). The FOM is
106 computationally expensive but provides the highest fidelity, while the RPM is computa-
107 tionally efficient but has low predictive fidelity. However, both models are physically consistent

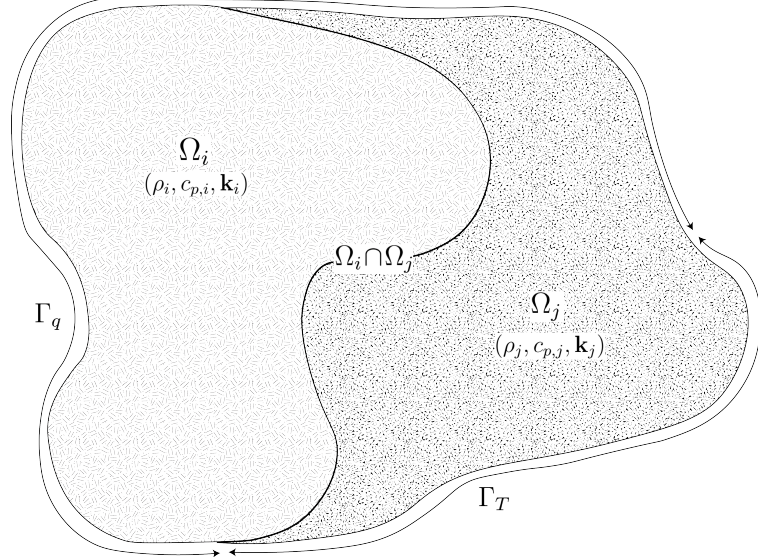


Figure 2: General domain Ω with prescribed Neumann and Dirichlet boundary conditions on Γ_q and Γ_T . Mesh displacement $w(x, t)$ occurs on the Γ_q boundary.

108 to high-dimensional design variables. The following discussion presents the TPS modeling
109 problem and the FOM and RPM solution strategies.

110 2.1 Governing Equations

111 The multi-physics of a non-decomposing ablating TPS under a hypersonic boundary layer
112 involves the *energy equation* for heat conduction inside the TPS, and the *pseudo-elasticity*
113 *equation* for mesh motion due to surface recession. The coupling between these two equations
114 occurs at the heated boundary, where the surface temperature drives the surface recession
115 velocity, which appears as an advection term in the energy equation. The governing PDEs
116 are described as follows.

117 2.1.1 Energy Equation

118 Consider a generic domain $\Omega \subset \mathbb{R}^d$, $d = 2$ or 3 , illustrated in Fig. 2. Let $\partial\Omega = \Gamma_q \cup \Gamma_T$
119 and $\Gamma_q \cap \Gamma_T = \emptyset$, where a Neumann $q_b(x, t)$ boundary condition is prescribed on the heated
120 boundary Γ_q , and represents the surface exposed to the hypersonic boundary layer. The
121 Dirichlet $T_b(x, t)$ boundary condition is prescribed on the boundary Γ_T . The TPS is divided
122 into N non-overlapping components $\{\Omega_i\}_{i=1}^N$, as illustrated in Fig. 2 for $N = 2$. The i -th
123 component Ω_i is associated with material properties $(\rho_i, c_{p,i}, \mathbf{k}_i)$, which are continuous within
124 one component, and can be discontinuous across two neighboring components.

125 The energy equation describes the transient heat conduction,

$$\rho c_p \left(\frac{\partial T}{\partial t} + \tilde{\mathbf{v}}(x, t) \cdot \nabla T \right) - \nabla \cdot (\mathbf{k} \nabla T) = 0, \quad x \in \Omega \quad (1a)$$

$$-\mathbf{k} \nabla T \cdot \mathbf{n} = q_b(x, t), \quad x \in \Gamma_q \quad (1b)$$

$$T(x, t) = T_b(x, t), \quad x \in \Gamma_T \quad (1c)$$

$$T(x, 0) = T_0(x), \quad x \in \Omega \quad (1d)$$

126 where ρ , c_p , and $\mathbf{k} \in \mathbb{R}^{d \times d}$ are the constant density, heat capacity, and thermal conductivity.
127 Note that our prior work has applied the PIROM to TPS problems with temperature-varying
128 material properties [17]. In the order they appear, the $\rho c_p \frac{\partial T}{\partial t}$ term includes the unsteady
129 energy storage, $\rho c_p \tilde{\mathbf{v}}(x, t) \cdot \nabla T$ includes the temperature advection due to ablation, and
130 $\nabla \cdot (\mathbf{k} \nabla T)$ includes the heat conduction. The boundary conditions for the energy equation
131 include Neumann eq. (1b) on Γ_q and Dirichlet eq. (1c) on Γ_T , and the initial condition is
132 provided in eq. (1d).

133 An Arbitrary Lagrangian-Eulerian (ALE) description is used to account for mesh motion
134 due to surface recession. The relative velocity of the material $\tilde{\mathbf{v}}(x, t)$ with respect to the
135 mesh is,

$$\tilde{\mathbf{v}}(x, t) = \mathbf{v}_s(x, t) - \mathbf{v}_m(x, t) \quad (2)$$

136 where $\mathbf{v}_s(x, t)$ and $\mathbf{v}_m(x, t)$ are the physical material velocity and mesh velocity, respectively.
137 In this work, the physical material velocity is assumed to be zero, i.e., $\mathbf{v}_s(x, t) = \mathbf{0}$, and thus
138 the relative velocity is simply the negative of the mesh velocity, $\tilde{\mathbf{v}}(x, t) = -\mathbf{v}_m(x, t)$.

139 2.1.2 Pseudo-Elasticity Equation

140 The mesh displacements $\mathbf{d} \in \mathbb{R}^d$ are described by the steady-state pseudo-elasticity equation,
141 which models the mesh as a fictitious elastic solid that deforms according to the prescribed
142 boundary displacements. The governing equation is given as,

$$\nabla \cdot \boldsymbol{\sigma}(\mathbf{d}) = \mathbf{0}, \quad \forall t \in \mathcal{T}, \quad x \in \Omega \quad (3a)$$

$$\mathbf{d}(x, t) = \mathbf{d}_q(x, t), \quad \forall t \in \mathcal{T}, \quad x \in \Gamma_q \quad (3b)$$

$$\mathbf{d}(x, t) = \mathbf{0}, \quad \forall t \in \mathcal{T}, \quad x \in \Gamma_T \quad (3c)$$

$$\mathbf{d}(x, 0) = \mathbf{0}, \quad \forall x \in \Omega \quad (3d)$$

143 where the stress tensor $\boldsymbol{\sigma}$ is related to the strain tensor $\boldsymbol{\epsilon}(\mathbf{d})$ through Hooke's law,

$$\boldsymbol{\sigma}(\mathbf{d}) = \mathbb{D} : \boldsymbol{\epsilon}(\mathbf{d})$$

144 where \mathbb{D} is the fourth-order positive definite elasticity tensor, and “ $:$ ” is the double con-
145 traction of the full-order tensor \mathbb{D} with the second-order tensor $\boldsymbol{\epsilon}$. The elasticity tensor
146 ordinarily possess a number of symmetries, effectively reducing the number of components
147 that describe it [2]. The symmetric strain tensor $\boldsymbol{\epsilon}$ measures the deformation of the mesh

148 due to displacements $\mathbf{d}(x, t)$, and is defined as,

$$\boldsymbol{\epsilon}(\mathbf{d}) = \frac{1}{2} (\nabla \mathbf{d} + \nabla \mathbf{d}^\top)$$

149 The “material” properties for the mesh are chosen to tailor the mesh deformation, and need
150 not represent the actual material being modeled [1].

151 For the pseudo-elasticity equations, the boundary conditions include prescribed displace-
152 ments $\mathbf{d}_q(x, t)$ on the heated boundary Γ_q in eq. (3b), and zero displacements on the unheated
153 boundaries in eq. (3c). The initial condition for the mesh displacements is zero in eq. (3d).
154 Particularly, the surface velocity due to the ablating material is a function of the surface
155 temperature $T_q(x, t)$ for $x \in \Gamma_q$ on the heated boundary. For the i -th material component,
156 the mesh velocity on the heated boundary is imposed based on the following relation,

$$\hat{\mathbf{n}} \cdot \mathbf{v}_m(x, t) = f_i(T_q(x, t)), \quad x \in \Gamma_q \quad (4)$$

157 where $\hat{\mathbf{n}}$ is the unit normal vector on the heated boundary Γ_q , and f_i is a material-dependent
158 function obtained from tabulated data, commonly referred to as a B’ table [1]. The B’ table
159 provides a model for the recession velocity as a function of the surface temperature, and is pre-
160 computed based on high-fidelity simulations or physical experiments for a one-dimensional
161 slab of materials, and is independent of the TPS geometry. Provided the surface velocity,
162 the boundary condition in eq. (5) for the mesh displacements are computed by integrating
163 the surface velocity over time,

$$\mathbf{d}_q(x, t) = \int_0^t \mathbf{v}_m(x, \tau) d\tau \quad (5)$$

164 2.2 Full-Order Model: Finite-Element Method

165 The following discussion presents the FOM for predicting the transient thermo-ablative re-
166 sponse of the TPS, based on a finite-element discretization of the governing equations in
167 eq. (1), including the energy equation and pseudo-elasticity equation.

168 **Energy Equation** To obtain the full-order numerical solution, the *energy equation* is spa-
169 tially discretized using variational principles of the Discontinuous Galerkin (DG) method [5].
170 Note that the choice of DG approach is mainly for theoretical convenience, and is exclusively
171 performed on the energy equation, as it is the surface temperature that drives the ablation
172 process; the equivalence between DG and FEM is noted upon their convergence. Consider
173 a conforming mesh partition domain, where each element belongs to one and only one com-
174 ponent. Denote the collection of all M elements as $\{E_i\}_{i=1}^M$. In an element E_i , its shared
175 boundaries with another element E_j , Neumann BC, and Dirichlet BC are denoted as e_{ij} , e_{iq} ,
176 and e_{iT} , respectively. Lastly, $|e|$ denotes the length ($n_d = 2$) or area ($n_d = 3$) of a component
177 boundary e . For the i -th element, use a set of P trial functions, such as polynomials, to

178 represent the temperature distribution,

$$T_i(x, t) = \sum_{l=1}^P \phi_l^i(x) u_l^i(t) \equiv \boldsymbol{\phi}_i^\top(x) \mathbf{u}(t), \quad i = 1, 2, \dots, M \quad (6)$$

179 Then, the energy equation is collected into a block-system of ODEs for all the elements in
180 the mesh,

$$\mathbf{A}\dot{\mathbf{u}} = [\mathbf{B} + \mathbf{C}(\mathbf{u})] \mathbf{u} + \mathbf{f}(t) \quad (7)$$

181 where $\mathbf{u} = [\mathbf{u}_1, \mathbf{u}_2, \dots, \mathbf{u}_M]^\top \in \mathbb{R}^{MP}$ includes all the DG variables, $\mathbf{f} \in \mathbb{R}^{MP}$ is the external
182 forcing, and the system matrices \mathbf{A} , \mathbf{B} , and \mathbf{C} are the matrices due to heat capacity, heat
183 conduction, and temperature advection due to mesh motion, respectively. Note that the
184 advection matrix $\mathbf{C}(\mathbf{u})$ is a function of the temperature \mathbf{u} since it depends on the mesh
185 velocity as in eq. (4); this is the main source of non-linearity in the current TPS problem.
186 A detailed derivation of eq. (7) and their matrices is provided in Appendix A.

187 **Pseudo-Elasticity Equation** The *pseudo-elasticity equation* is spatially discretized using
188 the standard Galerkin FEM method as implemented in the SIERRA mechanics module on a
189 structured mesh with quadrilateral elements [2]. Define the scalar basis functions $\{\psi_q(x)\}_{q=1}^Q$
190 nodal variables $\{\mathbf{d}_q\}_{q=1}^Q$ for the mesh displacements, where Q is the number of basis functions.
191 Express the mesh displacements \mathbf{w} at time t as,

$$\mathbf{w}(x, t) \approx \sum_{q=1}^Q \psi_q(x) \mathbf{w}_q \quad (8)$$

192 Substituting into the Galerkin weak form of the *steady* pseudo-elasticity equation, the fol-
193 lowing linear system of equations is obtained for the nodal displacements,

$$\mathbf{K}\mathbf{w} = \mathbf{g} \quad (9)$$

194 where \mathbf{w} is the global displacement vector, $\mathbf{K} \in \mathbb{R}^{dQ \times dQ}$ the global stiffness matrix of dimen-
195 sion d , defined by the volume integrals over the domain Ω provided the elasticity tensor \mathbb{D} ,
196 and \mathbf{g} is the global force vector due to the Dirichlet boundary conditions on the heated Γ_q
197 and unheated Γ_T boundaries.

198 2.3 Reduced-Physics Model

199 The RPM for predicting the response of the ablating TPS consists of two components: (1)
200 *surface recession model* (SRM) and a *lumped capacitance model* (LCM). The SRM provides
201 a relation between the surface temperature and *one-dimensional* surface recession veloc-
202 ity based on pre-computed B' tables for the material, enabling the computation of *one-*
203 *dimensional* surface displacements. Provided the geometry changed induced by the surface
204 recession, the LCM predicts the average temperature inside each component of the TPS,
205 which are in turn used as low-fidelity estimates for the surface temperatures required by the
206 SRM. Therefore, the SRM and LCM are coupled to define the RPM, providing low-fidelity

207 estimates for temperatures and surface recessions of the ablating TPS.

208 2.3.1 Surface Recession Model

209 The mesh displacements \mathbf{d} are constrained to be *one-dimensional* on the heated boundary
210 Γ_q , i.e., $w_i(x, t) = \mathbf{d}(x, t) \cdot \hat{\mathbf{n}}$, where $\hat{\mathbf{n}}$ is the unit normal vector on the heated boundary
211 Γ_q . Displacements perpendicular to $\hat{\mathbf{n}}$ are assumed small and are neglected. Let $\mathbf{w} =$
212 $[w_1, w_2, \dots, w_{\tilde{N}}]^\top \in \mathbb{R}^{\tilde{N}}$ include the displacements for the \tilde{N} ablating components on the
213 heated boundary, where $\tilde{N} \leq N$. Then the SRM capturing the one-dimensional surface
214 recession for ablating materials is,

$$\dot{\mathbf{w}} = \boldsymbol{\Xi} \mathbf{u} - \tilde{\mathbf{f}} \quad (10)$$

215 where $\boldsymbol{\Xi} = \text{diag}(\alpha_1, \dots, \alpha_{\tilde{N}})$ and $\tilde{\mathbf{f}} = (\alpha_1 u_{0,1}, \dots, \alpha_{\tilde{N}} u_{0,\tilde{N}})^\top$. The constants α_i are small
216 material-dependent constants, determined from the B' table, and $u_{0,i}$ is the constant initial
217 temperature of the ablative component. The SRM provides a relation between the surface's
218 temperature and recession velocity, based on pre-computed B' tables for the material.

219 2.3.2 Lumped Capacitance Model

220 A general form of the LCM is provided in this section; details regarding the derivation for
221 the four-component TPS used in the results section are provided in Appendix A. Let Ω be
222 partitioned into N non-overlapping components $\{\Omega_i\}_{i=1}^N$, as illustrated in Fig. 2 for $N = 2$.
223 The domain Ω is a function of the surface displacements \mathbf{w} on the heated boundary Γ_q , and
224 thus the geometry of each component Ω_i is time-dependent. The LCM predicts the temporal
225 variation of average temperatures in multiple interconnected components [9]. From a point
226 of view of energy conservation, the LCM leads to the following system of first-order ODEs
227 for the average temperatures in the components,

$$\bar{\mathbf{A}}(\mathbf{w})\dot{\bar{\mathbf{u}}} = \bar{\mathbf{B}}(\mathbf{w})\bar{\mathbf{u}} + \bar{\mathbf{f}}(t) \quad (11)$$

228 Where the states and inputs,

$$\bar{\mathbf{u}} = [\bar{u}_1, \bar{u}_2, \dots, \bar{u}_N]^\top \in \mathbb{R}^N, \quad \bar{\mathbf{f}} = [\bar{f}_1, \bar{f}_2, \dots, \bar{f}_N]^\top \in \mathbb{R}^N \quad (12)$$

229 include the average temperatures $\bar{\mathbf{u}}$ and spatially-integrated inputs $\bar{\mathbf{f}}$ for the N components.
230 For $i, j = 1, 2, \dots, N$ the (i, j) -th elements of the $\bar{\mathbf{A}} \in \mathbb{R}^{N \times N}$, $\bar{\mathbf{B}} \in \mathbb{R}^{N \times N}$, and $\bar{\mathbf{f}} \in \mathbb{R}^N$
231 matrices are given by,

$$\bar{A}_i = \begin{cases} \int_{\Omega_i} \rho c_p d\Omega_i, & i = j \\ 0, & i \neq j \end{cases}, \quad \bar{B}_{ij} = \begin{cases} \sum_{j \in \mathcal{N}_i \cup \{T_b\}} \bar{B}_{ij}^i, & i = j \\ \bar{B}_{ij}^{(j)}, & i \neq j \end{cases}, \quad (13a)$$

$$\mathbf{f}_i = \begin{cases} |e_{iq}| \bar{q}_i + \frac{|e_{iT}|}{R_i} \bar{T}_i, & i = j \\ 0, & i \neq j \end{cases} \quad (13b)$$

²³² where,

$$\bar{q}_i = \frac{1}{|e_{iq}|} \int_{e_{iq}} q_b de_{iq}, \quad \bar{T}_i = \frac{1}{|e_{iT}|} \int_{e_{iT}} T_b de_{iT}, \quad \bar{B}_{ij}^i = -\frac{|e_{ij}|}{R_{ij}}, \quad \bar{B}_{ij}^j = \frac{|e_{ij}|}{R_{ij}} \quad (14)$$

²³³ where R_{ij} is the equivalent thermal resistance between two neighboring components Ω_i and
²³⁴ Ω_j , and R_i is the thermal resistance between component Ω_i and the Dirichlet boundary.
²³⁵ Note that the heat capacitances and thermal resistances are computed based on the current
²³⁶ geometry of each component, which is a function of the surface displacements \mathbf{w} on the
²³⁷ heated boundary Γ_q .

²³⁸ 2.3.3 Thermo-Ablative Reduced-Physics Model

²³⁹ The SRM and LCM are combined to define the RPM for predicting the thermo-ablative
²⁴⁰ response of the TPS under hypersonic boundary layers. Specifically, the RPM is defined as
²⁴¹ the LCM as in eq. (11), where the *geometry-dependent* matrices $\tilde{\mathbf{A}}$, $\tilde{\mathbf{B}}$, and $\tilde{\mathbf{f}}$ are updated
²⁴² at each time step based on the current displacements \mathbf{w} provided by the SRM. The RPM is
²⁴³ formally stated as,

$$\tilde{\mathbf{A}}(\mathbf{s})\dot{\mathbf{s}} = \tilde{\mathbf{B}}(\mathbf{s})\mathbf{s} + \tilde{\mathbf{F}}(t) \quad (15a)$$

$$\tilde{\mathbf{z}} = \mathbf{s} \quad (15b)$$

²⁴⁴ where the state $\mathbf{s} = [\bar{\mathbf{u}}, \mathbf{w}]^\top \in \mathbb{R}^{N+\tilde{N}}$ includes the *average temperature* and *one-dimensional*
²⁴⁵ *surface displacements*, and \tilde{N} is the number of ablating components with $\tilde{N} \leq N$. Moreover,
²⁴⁶ the observables are defined as $\mathbf{z} = [\bar{\mathbf{u}}, \mathbf{w}]^\top \in \mathbb{R}^{N+\tilde{N}}$. The matrices are given as,

$$\tilde{\mathbf{A}}(\mathbf{s}) = \begin{bmatrix} \bar{\mathbf{A}}(\mathbf{s}) & \mathbf{0} \\ \mathbf{0} & \mathbf{I} \end{bmatrix}, \quad \tilde{\mathbf{B}}(\mathbf{s}) = \begin{bmatrix} \bar{\mathbf{B}}(\mathbf{s}) & \mathbf{0} \\ \boldsymbol{\Xi} & \mathbf{0} \end{bmatrix}, \quad \tilde{\mathbf{F}}(t) = \begin{bmatrix} \bar{\mathbf{f}}(t) \\ -\tilde{\mathbf{f}} \end{bmatrix} \quad (16)$$

²⁴⁷ In the matrices $\tilde{\mathbf{A}}$ and $\tilde{\mathbf{B}}$, the surface displacements \mathbf{w} are used to define the dimensions for
²⁴⁸ the Ω_i component used in eqs. (13) and (14), thus effectively coupling the LCM and SRM.

²⁴⁹ 2.4 Summary of Modeling Approaches

²⁵⁰ The FOM (i.e., FEM) and RPM (i.e., LCM with SRM) are two different but mathematically
²⁵¹ connected solution strategies. Particularly, the LCM in eq. (11) not only resembles the
²⁵² functional form of the DG model in eq. (7), but can be viewed as a special case of the latter,
²⁵³ where the mesh partition is extremely coarse, and the trial and test functions are piece-wise
²⁵⁴ constants. This removes all spatial variations within each component, and neglects advection
²⁵⁵ effects due to mesh motion.

²⁵⁶ For example, consider the case where each component Ω_i is treated as one single element,
²⁵⁷ and each element employs one constant basis function $\phi_i = 1$. The DG-FEM model for the
²⁵⁸ i -th component simplifies to the scalar ODE,

$$\mathbf{A}^{(i)} = \bar{A}_i, \quad \mathbf{C}^{(i)} = 0, \quad \mathbf{B}_{ij}^{(i)} = -\sigma|e_{ij}|, \quad \mathbf{B}_{ij}^{(j)} = \sigma|e_{ij}|, \quad \mathbf{f}_i = |e_{iq}|\bar{q}_i + \sigma|e_{iT}|\bar{T}_i \quad (17)$$

259 Clearly, the LCM is a coarse zeroth-order DG model with the inverse of thermal resistance
260 chosen as the element-wise penalty factors. Or conversely, the DG model is a refined version
261 of LCM via hp -adaptation.

262 The FOM and RPM represent two extremes in the modeling fidelity and computational
263 cost spectrum. On one hand, the FOM is the most accurate but computationally expensive
264 to evaluate due to the fine mesh discretizations for both the temperature and displacement
265 fields, leading to possibly millions of state variables. On the other hand, the RPM considers
266 only the average temperature of the material, from which the displacements are obtained by
267 integrating the velocity. The coarsened representation of the temperature field significantly
268 reduces the number of state variables to only a few per component, and thus reducing the
269 computational cost. However, this sacrifices local temperature information that becomes
270 critical to properly capture higher-order effects due to mesh motion and thermal gradients
271 within each component. Thus, neither the FOM nor the RPM is an universal approach for
272 real-world analysis, design, and optimization tasks for ablating TPS, where thousands of
273 high-fidelity model evaluations may be necessary. This issue motivates the development of
274 the PIROM, which can achieve the fidelity of FOM at a computational cost close to the
275 RPM, while maintaining the generalizability to model parameters.

276 **3 Physics-Infused Reduced-Order Modeling**

277 The formulation of PIROM for ablating TPS starts by connecting the FOM, i.e., the DG-
278 FEM, and the RPM, i.e., the LCM, via a coarse-graining procedure. This procedure pin-
279 points the missing dynamics in the LCM when compared to DG-FEM. Subsequently, the
280 Mori-Zwanzig (MZ) formalism is employed to determine the model form for the missing dy-
281 namics in PIROM. Lastly, the data-driven identification of the missing dynamics in PIROM
282 is presented.

283 **3.1 Deriving the Reduced-Physics Model via Coarse-Graining**

284 The subsequent coarse-graining formulation is performed on the DG-FEM in eq. (7) to
285 derive the LCM in eq. (11). This process constraints the trial function space of a full-
286 order DG model to a subset of piece-wise constants, so that the variables \mathbf{u} , matrices \mathbf{A} ,
287 \mathbf{B} , and \mathbf{C} , and forcing vector \mathbf{f} are all approximated using a single state associated to the
288 average temperature. Note that the coarse-graining is exclusively performed on the thermal
289 dynamics, as it is the surface temperature that drives the one-dimensional recession via
290 the SRM. Hence, the coarse-graining of the mesh dynamics is not included in the following
291 procedure.

292 **3.1.1 Coarse-Graining of States**

293 Consider a DG model as in eq. (7) for M elements and an LCM as in eq. (11) for N compo-
294 nents; clearly $M \gg N$. Let $\mathcal{V}_j = \{i | E_i \in \Omega_j\}$ be the indices of the elements belonging to the
295 j -th component, so $E_i \in \Omega_j$ for all $i \in \mathcal{V}_j$. The number of elements in the j -th component is

²⁹⁶ $|\mathcal{V}_j|$. The average temperature on Ω_j is,

$$\bar{u}_j = \frac{1}{|\Omega_j|} \sum_{i \in \mathcal{V}_j} \int_{E^{(i)}} \boldsymbol{\phi}^{(i)}(x)^T \mathbf{u}^{(i)} d\Omega = \frac{1}{|\Omega_j|} \sum_{i \in \mathcal{V}_j} |E_i| \boldsymbol{\varphi}_i^{j\top} \mathbf{u}^{(i)}, \quad j = 1, 2, \dots, N \quad (18)$$

²⁹⁷ where $|\Omega_j|$ and $|E_i|$ denote the area ($d = 2$) or volume ($d = 3$) of component j and element ²⁹⁸ i , respectively. The orthogonal basis functions are defined as $\boldsymbol{\varphi}_i^{j\top} = [1, 0, \dots, 0]^\top \in \mathbb{R}^P$.

²⁹⁹ Conversely, given the average temperatures of the N components, $\bar{\mathbf{u}}$, the states of an ³⁰⁰ arbitrary element E_i is written as,

$$\mathbf{u}^{(i)} = \sum_{k=1}^N \boldsymbol{\varphi}_i^k \bar{u}_k + \delta \mathbf{u}^{(i)}, \quad i = 1, 2, \dots, M \quad (19)$$

³⁰¹ where $\boldsymbol{\varphi}_i^k = 0$ if $i \notin \mathcal{V}_k$, and $\delta \mathbf{u}^{(i)}$ represents the deviation from the average temperature and ³⁰² satisfies the orthogonality condition $\boldsymbol{\varphi}_i^{k\top} \delta \mathbf{u}^{(i)} = 0$ for all k .

³⁰³ Equations eqs. (18) and (19) are combined and written in matrix form as,

$$\bar{\mathbf{u}} = \boldsymbol{\Phi}^+ \mathbf{u}, \quad \mathbf{u} = \boldsymbol{\Phi} \mathbf{u} + \delta \mathbf{u} \quad (20)$$

³⁰⁴ where $\boldsymbol{\Phi} \in \mathbb{R}^{MP \times N}$ is a matrix of $M \times N$ blocks, with the (i, j) -th block as $\boldsymbol{\varphi}_i^j$, $\boldsymbol{\Phi}^+ \in \mathbb{R}^{N \times MP}$ ³⁰⁵ is the left inverse of $\boldsymbol{\Phi}$, with the (i, j) -th block as $\boldsymbol{\varphi}_i^{j+} = \frac{|E_i|}{|\Omega_j|} \boldsymbol{\varphi}_i^{j\top}$, and $\delta \mathbf{u}$ is the collection of ³⁰⁶ deviations. By their definitions, $\boldsymbol{\Phi}^+ \boldsymbol{\Phi} = \mathbf{I}$ and $\boldsymbol{\Phi}^+ \delta \mathbf{u} = \mathbf{0}$.

³⁰⁷ 3.1.2 Coarse-Graining of Dynamics

³⁰⁸ The dependence of the matrices with respect to the displacements \mathbf{w} is dropped to isolate ³⁰⁹ the analysis based on coarsened variables. Consider a function of states in the form of ³¹⁰ $\mathbf{M}(\mathbf{u}) \mathbf{g}(\mathbf{u})$, where $\mathbf{g} : \mathbb{R}^{MP} \rightarrow \mathbb{R}^{MP}$ is a vector-valued function, and $\mathbf{M} : \mathbb{R}^{MP} \rightarrow \mathbb{R}^{p \times MP}$ ³¹¹ is a matrix-valued function with an arbitrary dimension p . Define the projection matrix ³¹² $\mathbf{P} = \boldsymbol{\Phi} \boldsymbol{\Phi}^+$ and the projection operator \mathcal{P} as,

$$\begin{aligned} \mathcal{P} [\mathbf{M}(\mathbf{u}) \mathbf{g}(\mathbf{u})] &= \mathbf{M}(\mathbf{P}\mathbf{u}) \mathbf{g}(\mathbf{P}\mathbf{u}) \\ &= \mathbf{M}(\boldsymbol{\Phi}\bar{\mathbf{u}}) \mathbf{g}(\boldsymbol{\Phi}\bar{\mathbf{u}}) \end{aligned} \quad (21)$$

³¹³ so that the resulting function depends only on the average temperatures $\bar{\mathbf{u}}$. Correspondingly, ³¹⁴ the residual operator $\mathcal{Q} = \mathcal{I} - \mathcal{P}$, and $\mathcal{Q} [\mathbf{M}(\mathbf{u}) \mathbf{g}(\mathbf{u})] = \mathbf{M}(\mathbf{u}) \mathbf{g}(\mathbf{u}) - \mathbf{M}(\boldsymbol{\Phi}\bar{\mathbf{u}}) \mathbf{g}(\boldsymbol{\Phi}\bar{\mathbf{u}})$. When ³¹⁵ the function is not separable, the projection operator is simply defined as $\mathcal{P} [\mathbf{g}(\mathbf{u})] = \mathbf{g}(\mathbf{P}\mathbf{u})$.

³¹⁶ Subsequently, the operators defined above are applied to coarse-grain the dynamics. First, ³¹⁷ write the DG-FEM in eq. (7) as,

$$\dot{\mathbf{u}} = \mathbf{A}^{-1} \mathbf{B} \mathbf{u} + \mathbf{A}^{-1} \mathbf{C}(\mathbf{u}) \mathbf{u} + \mathbf{A}^{-1} \mathbf{f}(t) \quad (22)$$

³¹⁸ and multiply both sides by $\boldsymbol{\Phi}^+$ to obtain,

$$\boldsymbol{\Phi}^+ \dot{\mathbf{u}} = \boldsymbol{\Phi}^+ (\boldsymbol{\Phi}\bar{\mathbf{u}} + \delta \mathbf{u}) = \dot{\bar{\mathbf{u}}} = \boldsymbol{\Phi}^+ \mathbf{r}(\mathbf{u}, t) \quad (23)$$

319 Apply the projection operator \mathcal{P} and the residual operator \mathcal{Q} to the right-hand side to obtain,

$$\dot{\bar{\mathbf{u}}} = \mathcal{P} [\Phi^+ \mathbf{r}(\mathbf{u}, t)] + \mathcal{Q} [\Phi^+ \mathbf{r}(\mathbf{u}, t)] \equiv \mathbf{r}^{(1)}(\bar{\mathbf{u}}, t) + \mathbf{r}^{(2)}(\mathbf{u}, t) \quad (24)$$

320 where $\mathbf{r}^{(1)}(\bar{\mathbf{u}}, t)$ is resolved dynamics that depends on $\bar{\mathbf{u}}$ only, and $\mathbf{r}^{(2)}(\mathbf{u}, t)$ is the un-resolved
321 or residual dynamics. Detailed derivations and analysis of $\mathbf{r}^{(1)}(\bar{\mathbf{u}}, t)$ and $\mathbf{r}^{(2)}(\mathbf{u}, t)$ can be
322 found in the Appendix.

323 It follows from our previous work in Ref. [17] that the resolved dynamics is exactly the
324 LCM, where the advection term reduces to zero, i.e., $\bar{\mathbf{C}}(\bar{\mathbf{u}}) = \mathbf{0}$, as shown in the Appendix.
325 Using the notation from eq. (11), it follows that,

$$\begin{aligned} \mathbf{r}^{(1)}(\bar{\mathbf{u}}, t) &= \bar{\mathbf{A}}(\mathbf{w})^{-1} \bar{\mathbf{B}}(\mathbf{w}) \bar{\mathbf{u}} + \bar{\mathbf{A}}(\mathbf{w})^{-1} \bar{\mathbf{C}}(\bar{\mathbf{u}}) \bar{\mathbf{u}} + \bar{\mathbf{A}}(\mathbf{w})^{-1} \bar{\mathbf{f}}(\bar{\mathbf{u}}) \\ &= \bar{\mathbf{A}}(\mathbf{w})^{-1} \bar{\mathbf{B}}(\mathbf{w}) \bar{\mathbf{u}} + \bar{\mathbf{A}}^{-1} \bar{\mathbf{f}}(t) \end{aligned} \quad (25)$$

326 where the following relations hold,

$$\bar{\mathbf{A}}(\mathbf{w}) = \mathbf{W} (\Phi^+ \mathbf{A}(\mathbf{w})^{-1} \Phi)^{-1} \quad \bar{\mathbf{C}}(\bar{\mathbf{u}}) = \mathbf{0} \quad (26a)$$

$$\bar{\mathbf{B}}(\mathbf{w}) = \mathbf{W} \Phi^+ \mathbf{B}(\mathbf{w}) \Phi \quad \bar{\mathbf{f}}(t) = \mathbf{W} \Phi^+ \mathbf{f} \quad (26b)$$

327 where $\mathbf{W} \in \mathbb{R}^{N \times N}$ is a diagonal matrix with the i -th element as $[\mathbf{W}]_{ii} = |\mathcal{V}_k|$ if $i \in \mathcal{V}_k$.
328 The examination of the second residual term $\mathbf{r}^{(2)}(\mathbf{u}, t)$ in eq. (24) is shown in the Appendix,
329 and demonstrates that the physical sources of missing dynamics in the LCM include: the
330 approximation of non-uniform temperature within each component as a constant, and the
331 elimination of the advection term due to coarse-graining. In sum, the above results not
332 only show that the LCM is a result of coarse-graining of the full-order DG-FEM, but also
333 reveal the discrepancies between the LCM and the DG-FEM. These discrepancies propagate
334 into the SRM, which as a result of the averaging in the LCM formulation, under-predicts
335 the surface recession rates. In the subsequent section, the discrepancies in the LCM are
336 corrected to formulate the PIROM.

337 3.2 Physics-Infusion Via Mori-Zwanzig Formalism

338 The Mori-Zwanzig (MZ) formalism is an operator-projection technique used to derive ROMs
339 for high-dimensional dynamical systems, especially in statistical mechanics and fluid dy-
340 namics [13, 14, 15]. It provides an exact reformulation of a high-dimensional Markovian dy-
341 namical system, into a low-dimensional observable non-Markovian dynamical system. The
342 proposed ROM is subsequently developed based on the approximation to the non-Markovian
343 term in the observable dynamics. Particularly, eq. (24) shows that the DG-FEM dyna-
344 mics can be decomposed into the resolved dynamics $\mathbf{r}^{(1)}(\mathbf{u}, t)$ and the orthogonal dynamics
345 $\mathbf{r}^{(2)}(\mathbf{u}, t)$, in the sense of $\mathcal{P}\mathbf{r}^{(2)} = 0$. In this case, the MZ formalism can be invoked to ex-
346 press the dynamics $\bar{\mathbf{u}}$ in terms of $\bar{\mathbf{u}}$ alone as the projected Generalized Langevin Equation
347 (GLE) [13, 14, 15],

$$\dot{\bar{\mathbf{u}}}(t) = \mathbf{r}^{(1)}(\bar{\mathbf{u}}, t) + \int_0^t \tilde{\boldsymbol{\kappa}}(t, s, \bar{\mathbf{u}}) ds \quad (27)$$

348 where the first and second terms are referred to as the Markovian and non-Markovian terms,
 349 respectively. The non-Markovian term accounts for the effects of past un-resolved states on
 350 the current resolved states via a memory kernel $\tilde{\kappa}(t, s, \bar{\mathbf{u}})$, which in practice is computationally
 351 expensive to evaluate.

352 3.2.1 Markovian Reformulation

353 This section details the formal derivation of the PIROM as a system of ODEs for the thermal
 354 dynamics, based on approximations to the memory kernel. Specifically, the kernel $\tilde{\kappa}$ is
 355 examined via a leading-order expansion, based on prior work [19]; this can be viewed as an
 356 analog of zeroth-order holding in linear system theory with a sufficiently small time step. In
 357 this case, the memory kernel is approximated as,

$$\tilde{\kappa}(t, s, \bar{\mathbf{u}}) \approx \mathbf{r}^{(1)}(\bar{\mathbf{u}}, t) \cdot \nabla_{\bar{\mathbf{u}}} \mathbf{r}^{(2)}(\Phi \bar{\mathbf{u}}, t) \quad (28)$$

358 Note that the terms in $\mathbf{r}^{(1)}$ have a common factor $\bar{\mathbf{A}}^{-1}$; this motivates the following heuristic
 359 modification of the model form in eq. (27),

$$\dot{\bar{\mathbf{u}}} = \mathbf{r}^{(1)}(\bar{\mathbf{u}}, t) + \bar{\mathbf{A}}(\mathbf{w})^{-1} \int_0^t \kappa(t, s, \bar{\mathbf{u}}) ds \quad (29a)$$

$$\bar{\mathbf{A}}(\mathbf{w}) \dot{\bar{\mathbf{u}}} = \bar{\mathbf{B}}(\mathbf{w}) \bar{\mathbf{u}} + \bar{\mathbf{f}}(t) + \int_0^t \kappa(t, s, \bar{\mathbf{u}}) ds \quad (29b)$$

360 where the original kernel $\tilde{\kappa}$ is effectively normalized by $\bar{\mathbf{A}}(\mathbf{w})^{-1}$. Intuitively, such choice
 361 of kernel reduces its dependency on the averaged material properties, and simplifies the
 362 subsequent design of model form.

363 Subsequently, the hidden states are introduced to “Markovianize” the system eq. (27).
 364 In this manner, eq. (29b) is converted into a pure state-space model, with the functional
 365 form of the LCM retained; since LCM is a physics-based model, then it encodes the phys-
 366 ical information and retains explicit parametric dependence of the problem. Consider the
 367 representation of the kernel as a finite sum of simpler functions, e.g., exponentials,

$$\kappa(t, s, \bar{\mathbf{u}}) = \sum_{j=1}^m \mathcal{K}_j(t, s, \bar{\mathbf{u}}) [\mathbf{p}_j + \mathbf{d}_j(\bar{\mathbf{u}})] \phi_j(s, \bar{\mathbf{u}}) \quad (30)$$

368 where,

$$\mathcal{K}_j(t, s, \bar{\mathbf{u}}) = e^{-\int_s^t (\lambda_j + e_j(\bar{\mathbf{u}})) d\tau}, \quad \phi_j(s, \bar{\mathbf{u}}) = \mathbf{q}_j^\top \bar{\mathbf{u}}(s) + \mathbf{g}_j(\bar{\mathbf{u}})^\top \bar{\mathbf{u}}(s) + \mathbf{r}_j^\top \bar{\mathbf{f}}(s) \quad (31)$$

369 with suitable coefficients $\mathbf{p}_j, \mathbf{d}_j, \mathbf{q}_j, \mathbf{g}_j, \mathbf{r}_j \in \mathbb{R}^N$ and decay rates $\lambda_j, e_j(\bar{\mathbf{u}}) > 0$, that need to
 370 be identified from data.

371 Define the hidden states as,

$$\beta_j(t) = \int_0^t \mathcal{K}_j(s, \bar{\mathbf{u}}) \phi_j(s, \bar{\mathbf{u}}) ds \quad (32)$$

³⁷² and differentiate with respect to time,,

$$\dot{\beta}_j(t) = -[\lambda_j + e_j(\bar{\mathbf{u}})]\beta_j(t) + \mathbf{q}_j^\top \bar{\mathbf{u}}(t) + \mathbf{g}_j(\bar{\mathbf{u}})^\top \bar{\mathbf{u}}(t) + \mathbf{r}_j^\top \bar{\mathbf{f}}(t) \quad (33)$$

³⁷³ to obtain the memory,

$$\int_0^t \boldsymbol{\kappa}(t, s, \bar{\mathbf{u}}) ds = \sum_{j=1}^m [\mathbf{p}_j + \mathbf{d}_j(\bar{\mathbf{u}})] \beta_j(t) \quad (34)$$

³⁷⁴ Then, eq. (29b) is recast as the extended Markovian system,

$$\bar{\mathbf{A}}(\mathbf{w})\dot{\bar{\mathbf{u}}} = \bar{\mathbf{B}}(\mathbf{w})\bar{\mathbf{u}} + [\mathbf{P} + \mathbf{D}(\bar{\mathbf{u}})]\boldsymbol{\beta} + \bar{\mathbf{f}}(t) \quad (35a)$$

$$\dot{\boldsymbol{\beta}} = [\mathbf{Q} + \mathbf{G}(\bar{\mathbf{u}})]\bar{\mathbf{u}} + [\mathbf{E}(\bar{\mathbf{u}}) - \boldsymbol{\Lambda}]\boldsymbol{\beta} + \mathbf{R}\bar{\mathbf{f}}(t) \quad (35b)$$

³⁷⁵ where the data-driven operators associated to the hidden dynamics are collected as,

$$\boldsymbol{\Lambda} = \text{diag}[\lambda_1, \lambda_2, \dots, \lambda_m] \in \mathbb{R}^{m \times m}, \quad \mathbf{P} = [\mathbf{p}_1, \mathbf{p}_2, \dots, \mathbf{p}_m] \in \mathbb{R}^{N \times m} \quad (36a)$$

$$\mathbf{D}(\bar{\mathbf{u}}) = [\mathbf{d}_1(\bar{\mathbf{u}}), \mathbf{d}_2(\bar{\mathbf{u}}), \dots, \mathbf{d}_m(\bar{\mathbf{u}})] \in \mathbb{R}^{N \times m}, \quad \mathbf{Q} = [\mathbf{q}_1, \mathbf{q}_2, \dots, \mathbf{q}_m] \in \mathbb{R}^{m \times N} \quad (36b)$$

$$\mathbf{G}(\bar{\mathbf{u}}) = [\mathbf{g}_1(\bar{\mathbf{u}}), \mathbf{g}_2(\bar{\mathbf{u}}), \dots, \mathbf{g}_m(\bar{\mathbf{u}})] \in \mathbb{R}^{m \times N}, \quad \mathbf{R} = [\mathbf{r}_1, \mathbf{r}_2, \dots, \mathbf{r}_m] \in \mathbb{R}^{m \times N} \quad (36c)$$

$$\mathbf{E}(\bar{\mathbf{u}}) = \text{diag}[e_1(\bar{\mathbf{u}}), e_2(\bar{\mathbf{u}}), \dots, e_m(\bar{\mathbf{u}})] \in \mathbb{R}^{m \times m} \quad (36d)$$

³⁷⁶ The form of the temperature-dependent matrices $\mathbf{D}(\bar{\mathbf{u}})$, $\mathbf{G}(\bar{\mathbf{u}})$, and $\mathbf{E}(\bar{\mathbf{u}})$ is specified in the
³⁷⁷ next section. Since the hidden states $\boldsymbol{\beta}$ serve as the memory, their initial conditions are set
³⁷⁸ to zero, i.e., $\boldsymbol{\beta}(t_0) = \mathbf{0}$, no memory at the beginning. The physics-infused model in eq. (35)
³⁷⁹ retains the structure of the LCM and depend on the displacements \mathbf{w} , while the hidden states
³⁸⁰ account for missing physics through corrections to the stiffness and advection matrices, as
³⁸¹ well as the forcing term.

³⁸² 3.2.2 Coupled Physics-Infused Model

³⁸³ The next step involves coupling the physics-infused model in eq. (35) with the SRM in
³⁸⁴ eq. (10) to define the PIROM for ablating TPS. To this end, define the surface temperature
³⁸⁵ $\mathbf{z}_u \in \mathbb{R}^{\tilde{N}}$ and displacements $\mathbf{z}_w \in \mathbb{R}^{\tilde{N}}$ for $\tilde{N} \leq N$ ablating components so that the observable
³⁸⁶ is given by $\mathbf{z} = [\mathbf{z}_u, \mathbf{z}_w]^\top \in \mathbb{R}^{n_z}$ with $n_z = 2\tilde{N}$ as the total number of observables.

³⁸⁷ Collect the RPM and hidden states into a single state vector $\mathbf{y} = [\bar{\mathbf{u}}, \mathbf{w}, \boldsymbol{\beta}]^\top \in \mathbb{R}^{n_y}$, where
³⁸⁸ $n_y = N + \tilde{N} + m$, and define a data-driven operator $\mathbf{M} \in \mathbb{R}^{n_z \times n_y}$ to define the PIROM's
³⁸⁹ observable as,

$$\mathbf{z} = \mathbf{My} \quad (37)$$

³⁹⁰ where,

$$\mathbf{M} = \begin{bmatrix} \mathbf{M}_{\bar{u}} & \mathbf{0} & \mathbf{M}_{\boldsymbol{\beta}} \\ \mathbf{0} & \mathbf{I} & \mathbf{0} \end{bmatrix} \quad (38)$$

³⁹¹ includes the matrices $\mathbf{M}_{\bar{u}} \in \mathbb{R}^{\tilde{N} \times N}$ and $\mathbf{M}_{\boldsymbol{\beta}} \in \mathbb{R}^{\tilde{N} \times m}$, which computes the surface tempera-
³⁹² ture observable from the RPM states and hidden states, respectively. The PIROM is coupled
³⁹³ to the SRM in eq. (10) by leveraging eq. (37) to compute the surface recession velocity. Thus,

³⁹⁴ the PIROM is formally stated as,

$$\mathcal{A}\dot{\mathbf{y}} = [\mathcal{B} + \mathcal{C}] \mathbf{y} + \mathcal{F}(t) \quad (39a)$$

$$\mathbf{z} = \mathbf{M}\mathbf{y} \quad (39b)$$

³⁹⁵ where,

$$\mathcal{A} = \begin{bmatrix} \bar{\mathbf{A}}(\mathbf{w}) & \mathbf{O} & \mathbf{O} \\ \mathbf{O} & \mathbf{I} & \mathbf{O} \\ \mathbf{O} & \mathbf{O} & \mathbf{I} \end{bmatrix} \in \mathbb{R}^{n_y \times n_y}, \quad \mathcal{B} = \begin{bmatrix} \bar{\mathbf{B}}(\mathbf{w}) & \mathbf{O} & \mathbf{P} \\ \Xi\mathbf{M}_u & \mathbf{O} & \Xi\mathbf{M}_\beta \\ \mathbf{Q} & \mathbf{O} & -\Lambda \end{bmatrix} \in \mathbb{R}^{n_y \times n_y}, \quad (40a)$$

$$\mathcal{C} = \begin{bmatrix} \mathbf{O} & \mathbf{O} & \mathbf{D}(\bar{\mathbf{u}}) \\ \mathbf{O} & \mathbf{O} & \mathbf{O} \\ \mathbf{G}(\bar{\mathbf{u}}) & \mathbf{O} & \mathbf{E}(\bar{\mathbf{u}}) \end{bmatrix} \in \mathbb{R}^{n_y \times n_y}, \quad \mathcal{F} = \begin{bmatrix} \bar{\mathbf{f}}(t) \\ -\tilde{\mathbf{f}} \\ \mathbf{R}\bar{\mathbf{f}}(t) \end{bmatrix} \in \mathbb{R}^{n_y} \quad (40b)$$

³⁹⁶ The learnable parameters in the PIROM are collected as,

$$\Theta = \{\mathbf{P}, \Lambda, \mathbf{Q}, \mathbf{M}, \mathbf{D}(\bar{\mathbf{u}}), \mathbf{G}(\bar{\mathbf{u}}), \mathbf{E}(\bar{\mathbf{u}}), \mathbf{R}\}, \in \mathbb{R}^{n_\theta} \quad (41)$$

³⁹⁷ The matrices $\mathbf{P}, \Lambda, \mathbf{Q}, \mathbf{M}, \mathbf{R}$ are constants, and account for the effects of coarse-graining on
³⁹⁸ the stiffness, output, and forcing matrices. The matrices $\mathbf{D}(\bar{\mathbf{u}}), \mathbf{E}(\bar{\mathbf{u}}), \mathbf{G}(\bar{\mathbf{u}})$ are temperature-
³⁹⁹ dependent matrices, and account for the effects of coarse-graining on the advection matrix
⁴⁰⁰ due to mesh motion. Leveraging the DG-FEM formula for the advection matrix in eq. (56c)
⁴⁰¹ in the Appendix, and noting that the ablating velocity in eq. (4) imposes the boundary
⁴⁰² condition for the mesh motion, the state-dependent matrices for the i -th component are
⁴⁰³ written as,

$$\mathbf{D}(\bar{\mathbf{u}}) \approx \text{diag}[\dot{\mathbf{w}}] \mathbf{D}, \quad \mathbf{G}(\bar{\mathbf{u}}) \approx \mathbf{G} \text{diag}[\dot{\mathbf{w}}], \quad \mathbf{E}(\bar{\mathbf{u}}) \approx \text{diag} \left[\underbrace{\dot{\mathbf{w}}, \dots, \dot{\mathbf{w}}}_{\tilde{m} \text{ times}} \right] \mathbf{E} \quad (42)$$

⁴⁰⁴ where $\dot{\mathbf{w}} = \dot{\mathbf{w}}(\bar{\mathbf{u}})$ is the SRM based on the observable temperature $\bar{\mathbf{u}}$ and \tilde{m} is the number
⁴⁰⁵ of hidden states per component so that $m = N\tilde{m}$.

⁴⁰⁶ The PIROM in eq. (39) incorporates explicit information on the material properties,
⁴⁰⁷ boundary conditions, and surface recession, and is designed to generalize across parametric
⁴⁰⁸ variations in these inputs. Moreover, the hidden dynamics in eq. (35) are interpretable, as
⁴⁰⁹ these retain the functional form of the DG-FEM in eq. (7). The next step is focused on
⁴¹⁰ identifying the unknown data-driven parameters Θ characterizing the hidden dynamics.

⁴¹¹ 3.3 Learning the Hidden Dynamics

⁴¹² Learning of the PIROM is achieved through a gradient-based neural-ODE-like approach [3].
⁴¹³ For ease of presentation, consider the compact form of the PIROM in eq. (39),

$$\mathcal{D}(\dot{\mathbf{y}}, \mathbf{y}, \xi, \mathcal{F}; \Theta) = \mathbf{0} \quad (43)$$

⁴¹⁴ where $\boldsymbol{\xi}$ defines the model parameters, i.e., material properties and B' tables, while \mathcal{F} ⁴¹⁵ represents the forcing terms, i.e., the boundary conditions.

⁴¹⁶ Consider a dataset of N_s high-fidelity *surface temperature* observable trajectories \mathbf{z}_{HF} ,
⁴¹⁷ sampled at p time instances $\{t_k\}_{k=0}^{p-1}$, for different parameter settings $\{\boldsymbol{\xi}^{(l)}\}_{l=1}^{N_s}$ and forcing
⁴¹⁸ functions $\{\mathcal{F}^{(l)}(t)\}_{l=1}^{N_s}$. The dataset is expressed as,

$$\mathcal{D} = \left\{ \left(t_k, \mathbf{z}_{\text{HF}}^{(l)}(t_k), \boldsymbol{\xi}^{(l)}, \mathcal{F}^{(l)}(t_k) \right) \right\}_{l=1}^{N_s}, \quad k = 0, 1, \dots, p - 1 \quad (44)$$

⁴¹⁹ In this work, the dataset contains only surface temperature observables – all high-fidelity
⁴²⁰ information regarding the surface displacements *are assumed to be unavailable during learning*.
⁴²¹

⁴²² The learning problem is formulated as the following differentially-constrained problem,

$$\min_{\Theta} \quad \mathcal{J}(\Theta; \mathcal{D}) = \sum_{l=1}^{N_s} \int_{t_0}^{t_f} \ell \left(\mathbf{z}_u^{(l)}, \mathbf{z}_{\text{HF}}^{(l)} \right) dt \quad (45a)$$

$$\text{s.t.} \quad \mathbf{0} = \mathcal{D} \left(\dot{\mathbf{y}}^{(l)}, \mathbf{y}^{(l)}, \boldsymbol{\xi}^{(l)}, \mathcal{F}^{(l)}; \Theta \right) \quad (45b)$$

⁴²³ for $l = 1, 2, \dots, N_s$, the objective is to minimize the discrepancy between the high-fidelity
⁴²⁴ and PIROM predictions for the l -th trajectory with $\ell \left(\mathbf{z}_u^{(l)}, \mathbf{z}_{\text{HF}}^{(l)} \right) = \left\| \mathbf{z}_u^{(l)} - \mathbf{z}_{\text{HF}}^{(l)} \right\|_2^2$.

⁴²⁵ The gradient-based optimization loop is based on the adjoint variable $\boldsymbol{\lambda}$, governed by the
⁴²⁶ adjoint differential equation,

$$\frac{\partial \ell}{\partial \mathbf{y}} + \boldsymbol{\lambda}^\top \frac{\partial \mathcal{D}}{\partial \mathbf{y}} - \frac{d}{dt} \left(\boldsymbol{\lambda}^\top \frac{\partial \mathcal{D}}{\partial \dot{\mathbf{y}}} \right) = \mathbf{0} \quad (46a)$$

$$\boldsymbol{\lambda}(t_f)^\top \frac{\partial \mathcal{D}}{\partial \dot{\mathbf{y}}(t_f)} = \mathbf{0} \quad (46b)$$

⁴²⁷ Once $\boldsymbol{\lambda}$ is solved, the gradient is computed as,

$$\nabla_\Theta \mathcal{J} = \frac{1}{N_s} \sum_{l=1}^{N_s} \int_{t_0}^{t_f} \left(\frac{\partial \ell}{\partial \Theta} + \left(\boldsymbol{\lambda}^{(l)} \right)^\top \frac{\partial \mathcal{D}}{\partial \Theta} \right) dt \quad (47)$$

⁴²⁸ 4 Application to Thermal Protection Systems

⁴²⁹ In this section, the proposed PIROM approach is applied to the analysis of thermo-ablative
⁴³⁰ multi-layered hypersonic TPS. The performance of the PIROM is evaluated in terms of the
⁴³¹ three corners of the ITM in Fig. 1, based on parametric variations of boundary conditions and
⁴³² SRMs. The results show PIROM to be a promising candidate for the solution of the impos-
⁴³³ sible trinity of modeling, achieving RPM-level computational efficiency and generalizability,
⁴³⁴ while attaining high-fidelity model accuracy.

Component	w (cm)	h (cm)	ρ (kg/m ³)	c_p (J/kg·K)	k (W/m·K)	$\alpha \times 10^{-6}$ (m/s·K)
#1	0.3	0.03	160	1200	0.2	1
#2	0.3	0.03	1800	900	5	1
#3	0.3	0.03	300	1500	0.15	1
#4	0.9	0.03	1600	800	10	0

Table 1: Description of TPS components, including thickness h , density ρ , specific heat capacity c_p , thermal conductivity k , and SRM parameter α .

4.1 Problem Definition

Consider the two-dimensional TPS configuration shown in Fig. 3 with constant material properties within each layer, dimensions, and BCs listed in Table 1. Such configuration is representative of the TPS used for the initial concept 3.X vehicle in past studies [10], and involves two main layers: an outer ablative layer, and an inner substrate layer. The top ablative layer may be composed of different materials, such as PICA or Avcoat, while the substrate layer is typically made of a high-temperature resistant material, such as carbon-carbon composite [7]. The ablative layer, composed of $\tilde{N} = 3$ ablative components, is subjected to strong time-varying and non-uniform heating, while the substrate layer, composed of one non-ablative component, is insulated adiabatically at the outer surface; the total number of components is thus $N = 4$.

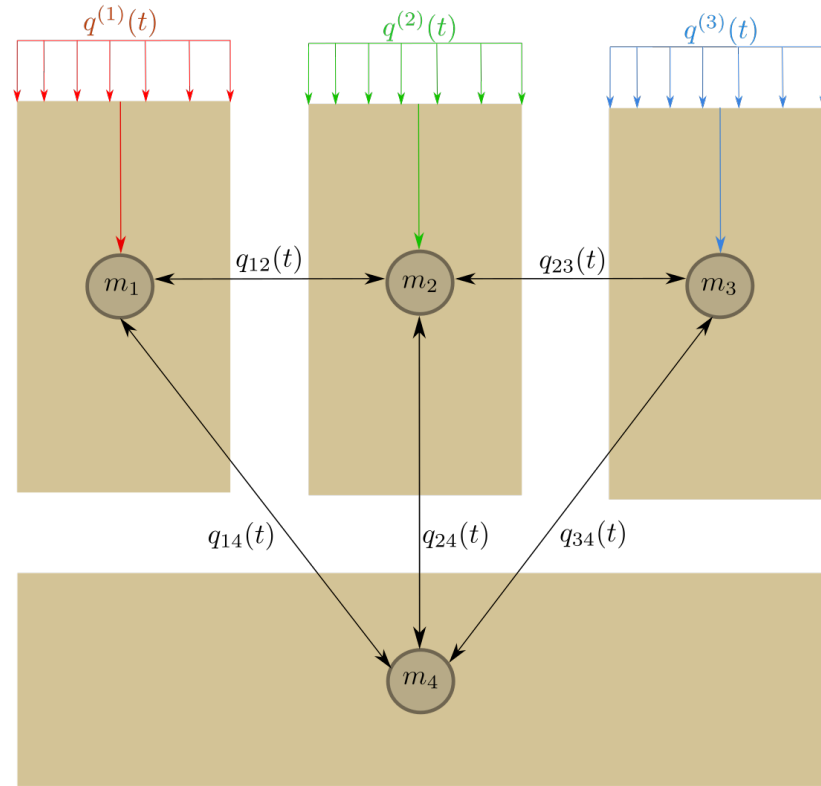
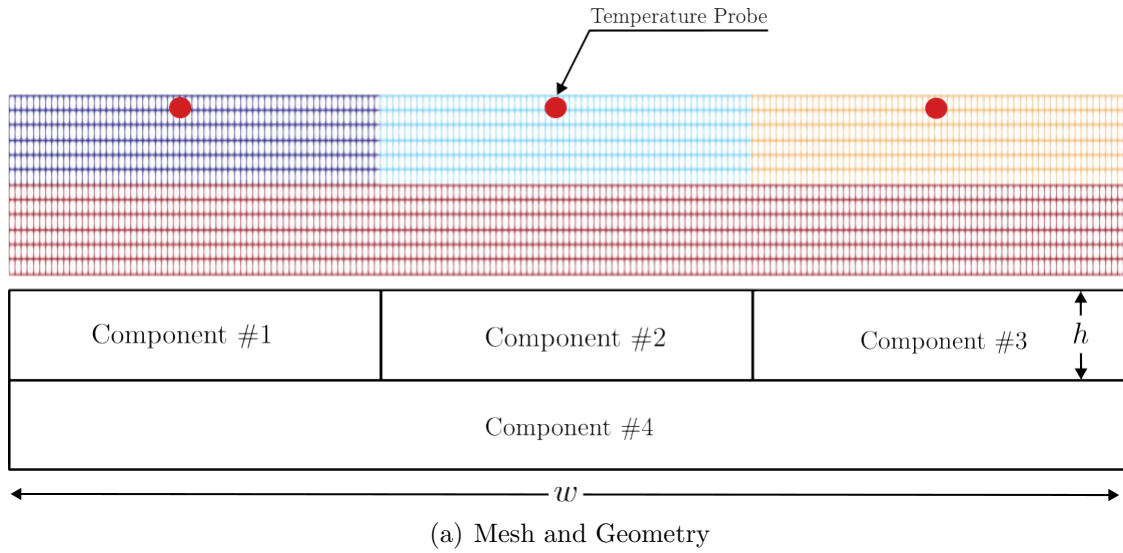
The lumped-mass representation of the TPS configuration is shown in Fig. 3(b), where each component Ω_i is represented by a lumped mass with uniform temperature $u_i(t)$. Details regarding the derivation of the LCM for this configuration are provided in Appendix A. The sources of non-linearities studied in this problem originate from the coupling between the thermodynamics and temperature-dependent mesh motion, i.e., geometry-dependent matrices, as well as the heterogeneities across material layers. As shown in Fig. 3, perfect thermocouple devices are placed at the surfaces of the ablative layers for the collection of the high-fidelity temperature signals that are used in the following sections for training and testing the PIROM.

4.2 Problem Parametrization

The operating conditions of the TPS are specified by the boundary conditions, i.e., the heat flux, and the surface recession model (SRM). Specifically, the heat flux on the Neumann BC is parametrized using $\boldsymbol{\xi}_{\text{BC}} = \{\xi_0, \xi_1, \xi_2\}$, while the SRM is parametrized using $\boldsymbol{\xi}_{\text{SRM}} = \{\alpha_1, \alpha_2, \alpha_3\}$. Thus, the heat flux and SRM over the i -th ablative component are expressed as,

$$q_i(x, t; \boldsymbol{\xi}_{\text{BC}}) = \xi_0 e^{\xi_1 x} e^{\xi_2 t}, \quad \forall x \in \Gamma_{i,q}, \quad \dot{w}_i(z_{u,i}; \boldsymbol{\xi}_{\text{SRM}}) = \alpha_i (z_{u,i} - u_{0,i}), \quad i = 1, \dots, \tilde{N} \quad (48)$$

where $\Gamma_{i,q}$, $z_{u,i}$, and $u_{0,i}$ correspond to the Neumann BC surface, the PIROM's surface temperature prediction, and the initial temperature of the i -th ablative component, respectively. The parameters ξ_0 , ξ_1 , and ξ_2 control the heat flux magnitude, spatial variation, and temporal variation, respectively. The constant α_i is a small material-dependent constant determined



(b) Lumped Mass Representation

Figure 3: Four-component TPS geometry and lumped-mass representation for the TPS.

465 from the B' table [12], specifying the surface recession velocity for a given temperature.

466 4.3 Data Generation

467 Full-order solutions of the TPS are computed using the FEM multi-mechanics module from
468 the **Aria** package [4], where the mesh is shown in Fig. 3. The mesh consists of 2196 total
469 elements, with 366 elements for each ablative component and 1098 elements for the sub-
470 strate component. Given an operating condition $\xi = [\xi_{\text{BC}}, \xi_{\text{SRM}}]^\top$, a high-fidelity solution
471 is computed for one minute, starting from an uniform initial temperature of $T(x, t_0) = 300$
472 K. Each solution consist of a collection of space-time-varying temperature and displacement
473 fields $\left\{ \left(t_k, \mathbf{u}_{\text{HF}}^{(l)}(t_k), \mathbf{d}_{\text{HF}}^{(l)}(t_k), \xi^{(l)} \right) \right\}_{k=0}^{p-1}$, where p is the number of time steps with a step size of
474 $\Delta t \approx 10^{-3}$. The observable trajectories are representative of near-wall thermocouple sensing
475 of hypersonic flows involving heat transfer. At each time instance t_k , a temperature reading
476 is recorded from each ablative component using the thermocouples shown in Fig. 3, resulting
477 in three temperature signals, i.e., the observables $\mathbf{z}_{\text{HF}} \in \mathbb{R}^3$. Therefore, each full-order solu-
478 tion produces one trajectory of observables $\left\{ \left(t_k, \mathbf{z}_{\text{HF}}^{(l)}(t_k), \xi^{(l)} \right) \right\}_{k=0}^{p-1}$. The goal of the PIROM
479 is to predict the surface temperature and displacement as accurately as possible.

480 4.3.1 Definition of Training and Testing Datasets

481 The range of parameters used to generate the training \mathcal{D}_1 and testing $\{\mathcal{D}_2, \mathcal{D}_3\}$ datasets
482 are listed in Table 1. The training and testing datasets are designed, respectively, to: (1)
483 minimize the information that the PIROM can “see”, and (2) to maximize the variabil-
484 ity of test operating conditions to examine the PIROM’s generalization performance. A
485 total of 110 normally-distributed data points for the BC parametrization are visualized in
486 Fig. 4(a), and the corresponding observable trajectories are shown in Figs. 4(b) and 4(c).
487 The training dataset \mathcal{D}_1 includes 10 trajectories with randomly selected BC parameters from
488 the 110 points, with nominal SRM parameters $\xi_{\text{SRM}} = \{1, 1, 1\} \times 10^{-6}$. Note that although
489 Fig. 4(c) shows the surface displacements for all ablative components in \mathcal{D}_1 , only the *surface*
490 *temperature is used for training the PIROM.*

491 Two additional datasets are generated for testing. The dataset \mathcal{D}_2 includes the remaining
492 100 BC parameter values not considered in \mathcal{D}_1 , and the high-fidelity simulation are generated
493 with the same nominal SRM parameters. The cases in the \mathcal{D}_3 fixes the boundary condition
494 as shown in Fig. 4(a) and varies the SRM parameters as shown in Table. 1. The testing
495 datasets \mathcal{D}_2 and \mathcal{D}_3 are *out-of-distribution* (OOD) datasets, and are meant for testing the
496 generalizability of the ROMs to unseen BCs and SRMs, respectively.

497 4.4 Performance Metrics

498 The performance of the PIROM is evaluated by the metrics of prediction error and computa-
499 tinoal cost.

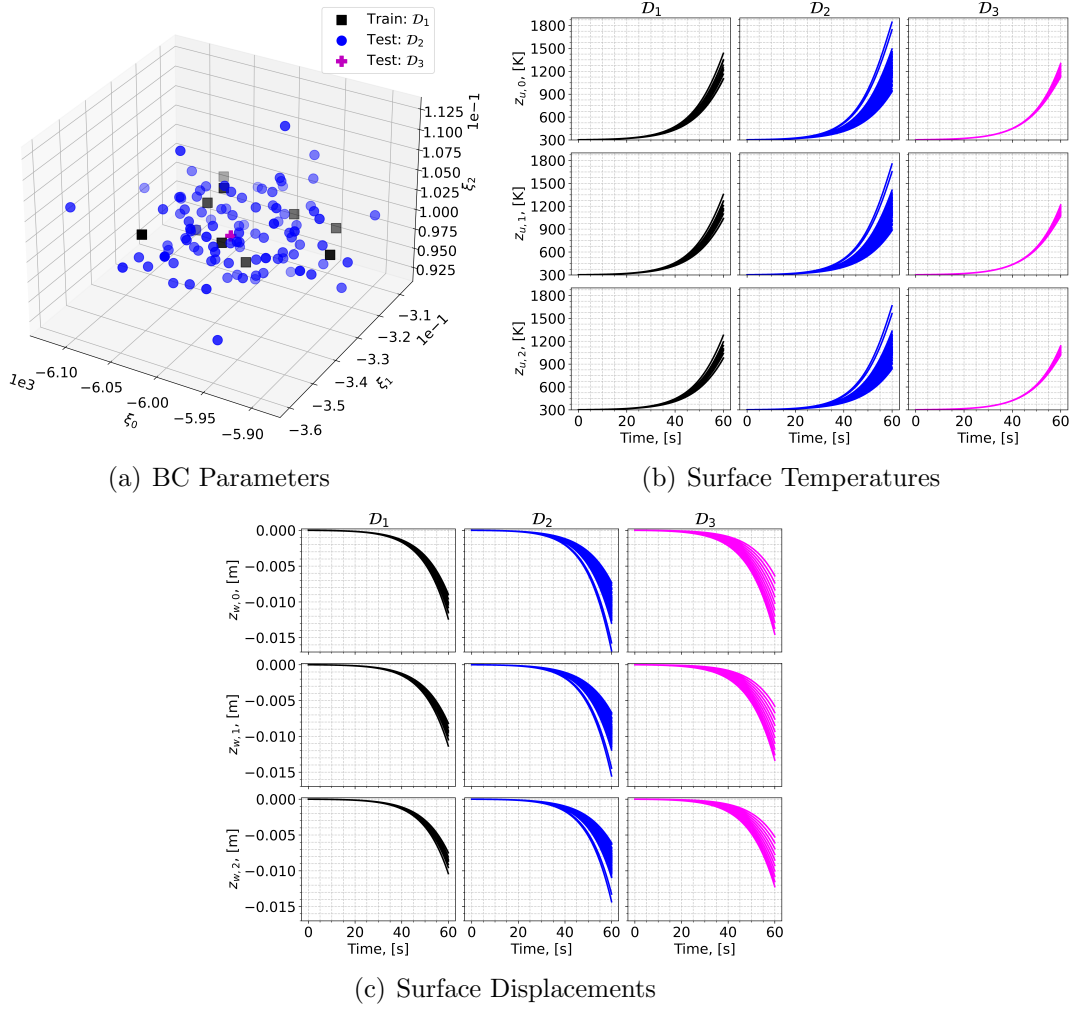


Figure 4: Boundary condition parameters, temperature observables, and displacement observables for the training and testing datasets. The variables $z_{u,i}$ and $z_{w,i}$ correspond to the surface temperature and displacement of the i -th ablative component, respectively.

500 **Prediction Error** Consider one trajectory of high-fidelity surface temperature and dis-
 501 placement data $\left\{ \left(t_k, \mathbf{z}_{u,\text{HF}}^{(l)}(t_k), \mathbf{z}_{w,\text{HF}}^{(l)}(t_k) \right) \right\}_{k=0}^{p-1}$ for the l -th operating condition in the testing
 502 datasets \mathcal{D}_2 or \mathcal{D}_3 . The difference $e_i^{(l)}$ for the i -th predicted observable, denoted as $z_i^{(l)}$, is
 503 computed as,

$$e_i^{(l)} = \frac{1}{\Delta z_i^{(l)}} \sqrt{\frac{1}{p} \sum_{k=0}^{p-1} \left(z_{i,\text{HF}}^{(l)}(t_k) - z_i^{(l)}(t_k) \right)^2} \quad (49)$$

504 for $i = 1, 2, 3$ and $z_i^{(l)} \in \{z_{i,u}^{(l)}, z_{i,w}^{(l)}\}$, and where,

$$\Delta z_i^{(l)} = \max_{0 \leq k \leq p-1} z_{i,\text{HF}}^{(l)}(t_k) - \min_{0 \leq k \leq p-1} z_{i,\text{HF}}^{(l)}(t_k) \quad (50)$$

505 Subsequently, the prediction error of one trajectory is computed by a weighted sum based
 506 on the area of each *ablative component*, resulting in the normalized root mean square error
 507 (NRMSE) metric for one trajectory,

$$\text{NRMSE} = \frac{\sum_{i=1}^{\tilde{N}} |\Omega_i| e_i^{(l)}}{\sum_{i=1}^{\tilde{N}} |\Omega_i|} \times 100\% \quad (51)$$

508 For one dataset, the NRMSE is defined to be the average of the NRMSEs of all trajectories
 509 in the dataset.

510 **Computational Acceleration** The *computational acceleration* metric focuses on the quan-
 511 tification of the speedup factor $\frac{\mathcal{T}_{\text{HF}}(\mathcal{D})}{\mathcal{T}_{\mathcal{M}}(\mathcal{D})}$, where $\mathcal{T}_{\text{HF}}(\mathcal{D})$ and $\mathcal{T}_{\mathcal{M}}(\mathcal{D})$ correspond to the wall-clock
 512 time required by the high-fidelity model and the reduced-order model \mathcal{M} (i.e., PIROM or
 513 RPM) to evaluate all trajectories in the dataset \mathcal{D} , respectively. For a benchmark analysis
 514 of the computational costs during the training phase, please refer to Ref. [17].

515 4.5 Generalization to Boundary Conditions

516 To assess generalization to BC, the PIROM and RPM are evaluated on the \mathcal{D}_2 dataset. Tem-
 517 perature trajectory predictions for a representative test case are shown in Figs. 5(a) and 5(b),
 518 where the PIROM accurately captures the surface temperature and displacement dynamics,
 519 while the RPM exhibits larger deviations and under-predicts surface displacements due to
 520 the averaging effects of the LCM. The mean NRMSE across all test cases in \mathcal{D}_2 is shown
 521 in Figs. 5(e) and 5(f), where the PIROM consistently achieves errors of $\approx 0.5\%$ for both
 522 temperature and displacement predictions, improving the RPM's accuracy by an order of
 523 magnitude. Figure 5 reports the average substrate temperature, where the LCM remains
 524 highly accurate due to the symmetric TPS geometry, adiabatic BCs, and negligible thermal
 525 gradients within the substrate. Although the PIROM is trained only on the surface tem-
 526 peratures of the three ablative components, its hidden dynamics retain the LCM's accuracy
 527 for this untrained observable, demonstrating the PIROM's ability to generalize and preserve
 528 the underlying physics of the reduced-physics backbone.

529 **4.6 Generalization to Surface Recession Models**

530 The generalization performance of the PIROM and RPM is also evaluated on surface recess-
531 sion models using the \mathcal{D}_3 dataset. As detailed in Table 1, the SRM parameter α in \mathcal{D}_3 is
532 perturbed 10 times by up to $\pm 50\%$ from their nominal values. The SRM model perturbation
533 introduces significant changes to the ablative layer dynamics, potentially increasing the rate
534 of ablation at lower temperatures, as shown in Figs. 5(c) and 5(d). The PIROM, without
535 considering any SRM variations during training, is able to accurately predict the surface tem-
536 perature and displacement dynamics for the perturbed SRMs. Figures 5(e) and 5(f) show
537 the mean NRMSE across all test cases in \mathcal{D}_3 , where the PIROM consistently achieves errors
538 below 1.5% for both temperature and displacement predictions, and consistently improves
539 the RPM’s accuracy by approximately an order of magnitude.

540 **4.7 Computational Cost**

541 All computations are performed in serial for fairness on an Intel Xeon (R) Gold 6258R
542 CPU 2.70GHz computer with 62 GB of RAM. The numerical integration for the RPM
543 and PIROM models are performed using SciPy’s `solve_ivp` function with default settings.
544 Provided a parametrization for the BC and SRM, the high-fidelity FEM simulation takes
545 about ≈ 60 seconds, the RPM takes about ≈ 0.137 seconds, and the PIROM takes about
546 ≈ 0.280 seconds. Therefore, during evaluation both the RPM and PIROM achieve speedup
547 factors of approximately 438 and 214, respectively, over the high-fidelity model. As a result,
548 the PIROM and RPM are *two-orders-of-magnitude faster* than the high-fidelity model. The
549 PIROM nearly preserves the computational efficiency of the RPM (about twice as expensive
550 as the RPM), while achieving significantly higher accuracy and generalization capabilities.
551 The results demonstrate the benefits of physics-infused modeling for the development of
552 efficient and generalizable ROMs for complex multi-physics systems.

553 **4.8 Summary of Results**

554 The results presented in this section demonstrate the accuracy, generalizability, and com-
555 putational efficiency of the proposed PIROM approach for the analysis of thermo-ablative
556 multi-layered hypersonic TPS. The PIROM consistently achieves low prediction errors below
557 1% for both surface temperature and displacement across a range of unseen boundary con-
558 ditions and surface recession models. Furthermore, the PIROM retains the computational
559 efficiency of traditional RPMs, achieving speedup factors of over 200 times compared to high-
560 fidelity FEM simulations. The generalization capabilities of the PIROM are attributed to its
561 hybrid structure: a physics-based LCM backbone that ensures consistency with the under-
562 lying thermodynamics, while a data-driven correction mechanism captures the un-resolved
563 dynamics.

564 **5 Conclusions**

565 This work presents the development and validation of the *scientific machine learning* frame-
566 work termed *Physics-Informed Reduced Order Model* (PIROM) for simulating the transient

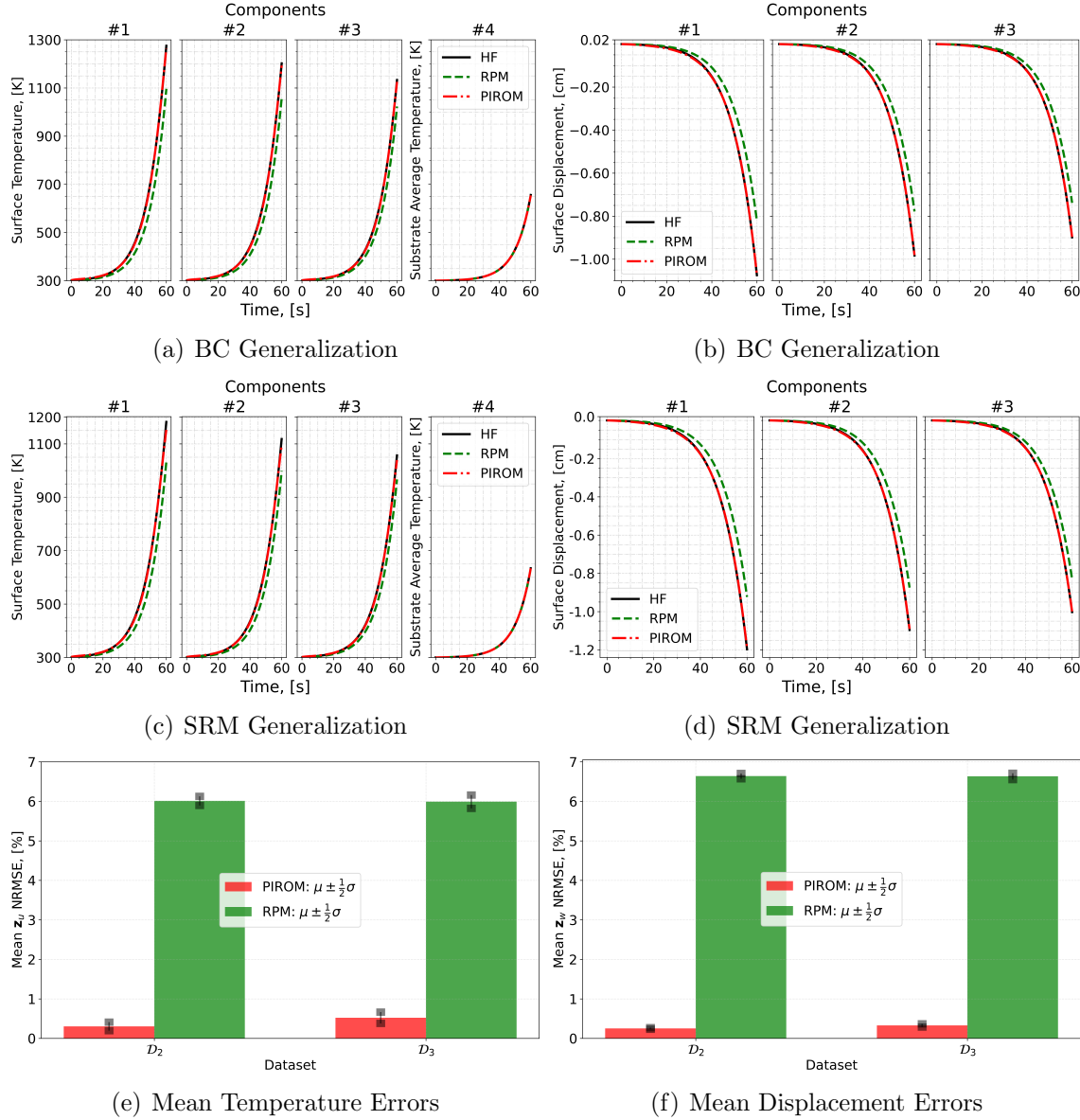


Figure 5: PIROM predictions against high-fidelity solutions for (a)-(b) BC generalization, (c)-(d) SRM generalization, and (e)-(f) mean errors across testing datasets.

567 thermo-ablative response of hypersonic thermal protection systems (TPS) subjected to hy-
568 personic aerodynamic heating. Using coarse-graining on a DG-FEM model and the Mori-
569 Zwanzig formalism, the PIROM formulation in Ref. [17] is extended to account for non-
570 decomposing ablative material response. The PIROM builds upon the following two key
571 components: (1) a first-order physics-based model, i.e., the LCM and SRM, for low-fidelity
572 predictions of the transient thermo-ablative TPS response; and (2) a data-driven closure to
573 the non-Markovian term in the generalized Langevin equation (GLE). The non-Markovian
574 closure is recast as a set of hidden states that evolve according to a data-driven dynamical
575 system that is learned from a sparse collection of high-fidelity temperature signals.

576 The results demonstrate that the PIROM framework effectively reconciles the trade-
577 offs between accuracy, generalizability, and efficiency of the ITM for simulating ablating
578 hypersonic TPS. The PIROM consistently achieves mean observable prediction errors of
579 $\approx 0.5\%$ for a wide range of extrapolative settings of model parameters, involving time-and-
580 space varying boundary conditions and SRM models. Notably, the PIROM improves the
581 RPM's accuracy by an order of magnitude while preserving its computational efficiency,
582 physical interpretability, and parametric generalizability. Moreover, the PIROM delivers
583 online evaluations that are two orders of magnitude faster than the FOM. These results
584 highlight the PIROM's potential as a promising framework for optimizing multi-physical
585 dynamical systems, such as TPS under diverse operating conditions.

586 A Technical Details

587 This appendix presents the technical details of the PIROM framework applied to the trans-
 588ient modeling of thermo-ablative TPS. The first section provides the mathematical details
 589 for the definition of the DG-FEM. The second section details the coarse-graining proce-
 590 dures performed on the DG-FEM representation of the TPS. The third section presents the
 591 derivation of the LCM model from an energy-conservation perspective.

592 A.1 Full-Order Model

593 To obtain the full-order numerical solution, the governing equation is spatially discretized
 594 using variational principles of Discontinuous Galerkin (DG) to result in a high-dimensional
 595 system of ordinary differential equations (ODEs). The DG-FEM model is written in an
 596 element-wise form, which is beneficial for subsequent derivations of the lower-order models.
 597 Note that the choice of DG approach here is mainly for theoretical convenience in the sub-
 598 sequent coarse-graining formulation. In the numerical results, the full-order TPS ablation
 599 simulations is computed using standard FEM instead, and the equivalence between DG and
 600 standard FEM is noted upon their convergence.

601 A.1.1 Domain Discretization

602 Consider a conforming mesh partition of the domain in Fig. 3, where each element belongs
 603 to one and only one component. Denote the collection of all M elements as $\{E_i\}_{i=1}^M$. To ease
 604 the description of the DG model, a graph structure is employed. The elements are treated
 605 as vertices, the set of which is denoted $\mathcal{V} = \{m\}_{m=1}^M$. Two neighboring elements, E_i and E_j ,
 606 are connected by an edge (i, j) , and the shared boundary between them is denoted e_{ij} . The
 607 collection of all edges are denoted \mathcal{E} , and \mathcal{G} is referred to as a graph. In the graph, the edges
 608 are unidirected, meaning if $(i, j) \in \mathcal{E}$ then $(j, i) \in \mathcal{E}$. Furthermore, denote the neighbors
 609 of the i -th element as $\mathcal{N}_i = \{j | (i, j) \in \mathcal{E}\}$. Lastly, for the ease of notation, introduce two
 610 special indices: T for the boundary of an element that overlaps with the Dirichlet boundary
 611 condition, and similarly q for the Neumann boundary condition.

612 A.1.2 Weak Form of Discontinuous Galerkin Method

613 Choosing appropriate basis functions ϕ_k and ϕ_l and using the Interior Penalty Galerkin
 614 (IPG) scheme [5], the variational bilinear form for eq. (1a) is,

$$\sum_{i=1}^M a_{\epsilon,i}(\phi_k, \phi_l) = \sum_{i=1}^M L_i(\phi_k) \quad (52)$$

615 where ϵ is an user-specified parameter and,

$$a_{\epsilon,i}(\phi_k, \phi_l) = \int_{E^{(i)}} \left(\rho c_p \phi_k \frac{\partial \phi_l}{\partial t} + \nabla \phi_k \cdot (\mathbf{k} \nabla \phi_l) - \rho c_p \phi_k \mathbf{v} \cdot \nabla \phi_l \right) dE^{(i)} \quad (53a)$$

$$\begin{aligned} &= - \sum_{j \in \mathcal{N}_i \cup \{T_b\}} \int_{e_{ij}} \{ \mathbf{k} \nabla \phi_k \cdot n \} [\phi_l] de_{ij} + \epsilon \sum_{j \in \mathcal{N}_i \cup \{T_b\}} \int_{e_{ij}} \{ \mathbf{k} \nabla \phi_l \cdot n \} [\phi_k] de_{ij} \\ &\quad + \sigma \sum_{j \in \mathcal{N}_i \cup \{T_b\}} \int_{e_{ij}} [\phi_k] [\phi_l] de_{ij} \end{aligned} \quad (53b)$$

$$L_i(v) = \epsilon \sum_{j \in \mathcal{N}_i \cup \{T_b\}} \int_{e_{ij}} (\mathbf{k} \nabla \phi_l \cdot n) T_b de_{ij} + \int_{e_{iq}} \phi_k q_b de_{iq} + \sigma \int_{e_{iT}} \phi_k T_b de_{iT} \quad (53c)$$

616 In the bi-linear form above, the notations $[]$ and $\{ \}$ are respectively the jumps and averages
617 at the boundary e_{ij} share by two elements E_i and E_j ,

$$[u] = u|_{E_i} - u|_{E_j}, \quad \{u\} = \frac{1}{2} \left(u|_{E_i} + u|_{E_j} \right), \quad \text{for } x \in e_{ij} = E_i \cap E_j$$

618 Furthermore, in the bi-linear form, the terms associated with σ are introduced to enforce
619 the Dirichlet boundary conditions; σ is a penalty factor whose value can depend on the size
620 of an element. Depending on the choice of ϵ , the bi-linear form corresponds to symmetric
621 IPG ($\epsilon = -1$), non-symmetric IPG ($\epsilon = 1$), and incomplete IPG ($\epsilon = 0$). All these schemes
622 are consistent with the original PDE and have similar convergence rate with respect to mesh
623 size. In the following derivations, the case $\epsilon = 0$ is chosen for the sake of simplicity.

624 A.1.3 Discontinuous Galerkin Model

625 Next, the DG-based model is written in an element-wise form. For the i -th element, use a
626 set of P trial functions to represent the temperature as in eq. (6). Without loss of generality,
627 the trial functions are assumed to be orthogonal, so that,

$$\int_{E_i} \phi_l^i(x) \phi_k^i(x) d\Omega = 0, \quad l \neq k$$

628 where $|E_i|$ is the area ($n_d = 2$) or volume ($n_d = 3$) of the i -th element, and δ_{lk} is the Kronecker
629 delta function. Furthermore, for simplicity, choose $\phi_1^i = 1$. Thus, by orthogonality,

$$\int_{E_i} \phi_1^i(x) d\Omega = |E_i|, \quad \int_{E_i} \phi_k^i(x) d\Omega = 0, \quad k = 2, 3, \dots, P$$

630 Under the choice of basis functions, u_1^i is simply the average temperature of element E_i ,
631 denoted as \bar{u}_i .

632 Using test functions same as trial functions, the dynamics $\mathbf{u}^{(i)}$ is obtained by evaluating
633 the element-wise bi-linear forms,

$$a_{\epsilon,i}(\phi_k^{(i)}, T^{(i)}) = L_i(\phi_k^{(i)}), \quad k = 1, 2, \dots, P \quad (54)$$

⁶³⁴ Therefore, by standard variational principles, e.g., [5], the element-wise governing equation
⁶³⁵ is denoted as,

$$\mathbf{A}_i \dot{\mathbf{u}}_i = (\mathbf{B}_i + \mathbf{C}_i) \mathbf{u}_i + \sum_{j \in \mathcal{N}_i \cup \{T_b\}} (\mathbf{B}_{ij}^i \mathbf{u}_i + \mathbf{B}_{ij}^j \mathbf{u}_j) + \mathbf{f}_i(t), \quad \text{for } i = 1, 2, \dots, M \quad (55)$$

⁶³⁶ where for $k, l = 1, 2, \dots, P$,

$$[\mathbf{A}^{(i)}]_{kl} = \int_{E^{(i)}} \rho c_p \phi_k^{(i)} \phi_l^{(i)} dE^{(i)} \quad (56a)$$

$$[\mathbf{B}^{(i)}]_{kl} = - \int_{E^{(i)}} (\nabla \phi_k^{(i)}) \cdot (\mathbf{k} \nabla \phi_l^{(i)}) dE^{(i)} \quad (56b)$$

$$[\mathbf{C}^{(i)}]_{kl} = \int_{E^{(i)}} \rho c_p \phi_k^{(i)} \mathbf{v}^{(i)} \cdot \nabla \phi_l^{(i)} dE^{(i)} \quad (56c)$$

$$[\mathbf{B}_{ij}^{(i)}] = \int_{e_{ij}} \left\{ \mathbf{k} \nabla \phi_k^{(i)} \cdot \hat{n} \right\} \phi_l^{(i)} - \sigma [\phi_k^{(i)}] \phi_l^{(i)} de_{ij} \quad (56d)$$

$$[\mathbf{B}_{ij}^{(j)}] = \int_{e_{ij}} - \left\{ \mathbf{k} \nabla \phi_k^{(i)} \cdot \hat{n} \right\} \phi_l^{(j)} + \sigma [\phi_k^{(i)}] \phi_l^{(j)} de_{ij} \quad (56e)$$

$$[\mathbf{f}^{(i)}]_k = \int_{e_{iq}} \phi_k^{(i)} q_b de_{iq} + \sigma \int_{e_{iT}} \phi_k^{(i)} de_{iT} \quad (56f)$$

⁶³⁷ The matrices $\mathbf{A}^{(i)} \in \mathbb{R}^{P \times P}$, $\mathbf{B}^{(i)} \in \mathbb{R}^{P \times P}$, and $\mathbf{C}^{(i)} \in \mathbb{R}^{P \times P}$ are respectively the capacitance,
⁶³⁸ conductivity, and advection matrices for element i . These matrices depend on ρ , c_p , \mathbf{k} , and
⁶³⁹ \mathbf{v} , and hence can be non-linear functions of $\mathbf{u}^{(i)}$. Since the trial functions are orthogonal, if
⁶⁴⁰ ρc_p is constant within an element, $\mathbf{A}^{(i)}$ is diagonal; otherwise, \mathbf{A}_i is symmetric and positive
⁶⁴¹ definite as $\rho c_p > 0$.

⁶⁴² For compactness, the element-wise model in eq. (55) is also written in matrix form,

$$\mathbf{A} \dot{\mathbf{u}} = [\mathbf{B} + \mathbf{C}(\mathbf{u})] \mathbf{u} + \mathbf{f}(t) \quad (57)$$

⁶⁴³ where $\mathbf{u} = [\mathbf{u}^{(1)}, \mathbf{u}^{(2)}, \dots, \mathbf{u}^{(M)}]^T \in \mathbb{R}^{MP}$ includes all DG variables, $\mathbf{f} = [\mathbf{f}^{(1)}, \mathbf{f}^{(2)}, \dots, \mathbf{f}^{(M)}]^T \in \mathbb{R}^{MP}$, \mathbf{A} and \mathbf{C} are matrices of M diagonal blocks whose i -th blocks are $\mathbf{A}^{(i)}$ and $\mathbf{C}^{(i)}$, and
⁶⁴⁴ \mathbf{B} is a matrix of $M \times M$ blocks whose (i, j) -th block is,

$$\mathbf{B}_{ij} = \begin{cases} \mathbf{B}^{(i)} + \sum_{j \in \mathcal{N}_i \cup \{T_b\}} \mathbf{B}_{ij}^{(i)}, & i = j \\ \mathbf{B}_{ij}^{(j)}, & i \neq j \end{cases} \quad (58)$$

⁶⁴⁶ The dependency of \mathbf{C} on \mathbf{u} is explicitly noted in eq. (57), which is the main source of non-
⁶⁴⁷ linearity in the current TPS problem. Moreover, the mesh velocity \mathbf{v} varies with space
⁶⁴⁸ and time, and thus the advection matrix \mathbf{C} varies with time as a function of the surface
⁶⁴⁹ temperature $T_q(x, t)$.

650 A.2 Coarse-Graining of Dynamics

651 The LCM is obtained by coarse-graining the full-order DG-FEM. This coarse-graining procedure produces resolved $\mathbf{r}^{(1)}(\mathbf{u}, t)$ and residual $\mathbf{r}^{(2)}(\mathbf{u}, t)$ dynamics as in eq. (24). This section 652 presents the detail derivations and magnitude analysis for the resolved and residual dynamics. 653

655 A.2.1 Resolved Dynamics

656 Using eq. (21), the resolved dynamics is computed as follows,

$$\mathbf{r}^{(1)}(\bar{\mathbf{u}}, t) = \mathcal{P} [\Phi^+ \mathbf{A}^{-1} (\mathbf{B}\mathbf{u} + \mathbf{C}(\mathbf{u})\mathbf{u} + \mathbf{f}(t))] \quad (59a)$$

$$= \Phi^+ \mathbf{A}^{-1} \mathbf{P} \mathbf{B} \mathbf{P} \mathbf{u} + \Phi^+ \mathbf{A}^{-1} \mathbf{P} \mathbf{C} (\mathbf{P} \mathbf{u}) \mathbf{P} \mathbf{u} + \Phi^+ \mathbf{A}^{-1} \mathbf{P} \mathbf{f}(t) \quad (59b)$$

$$= \underbrace{\Phi^+ \mathbf{A}^{-1} \Phi}_{\#1} \underbrace{\Phi^+ \mathbf{B} \Phi \bar{\mathbf{u}}}_{\#2} + \Phi^+ \mathbf{A}^{-1} \Phi \underbrace{\Phi^+ \mathbf{C} (\Phi \bar{\mathbf{u}}) \Phi}_{\#3} \bar{\mathbf{u}} + \Phi^+ \mathbf{A}^{-1} \Phi \underbrace{\Phi^+ \mathbf{f}(t)}_{\#4} \quad (59c)$$

657 Detailed derivations for the #1, #2, and #4 terms can be found in Ref. [17] for the case of 658 temperature-varying matrices. The effects of coarse-graining on the advection term #3 are 659 analyzed next.

660 **Term #3** The $\mathbf{C}(\mathbf{u}) \in \mathbb{R}^{MP \times MP}$ matrix contains M diagonal of size $P \times P$, since the 661 basis functions are defined locally on each element. Therefore, $[\mathbf{C}(\mathbf{u})]_{ij} = \mathbf{0}$ for all $i \neq j$ with 662 $i, j = 1, 2, \dots, M$. It follows that for $k, l = 1, 2, \dots, N$,

$$[\Phi^+ \mathbf{C}(\Phi \bar{\mathbf{u}}) \Phi]_{kl} = \sum_{i=1}^M \sum_{j=1}^M \varphi_i^{k+} [\mathbf{C}(\Phi \bar{\mathbf{u}})]_{ij} \varphi_j^l \quad (60a)$$

$$= \sum_{i=1}^M \varphi_i^{k+} [\mathbf{C}(\Phi \bar{\mathbf{u}})]_{ii} \varphi_i^l \quad (60b)$$

$$= \sum_{i \in \mathcal{V}_k} \varphi_i^{k+} [\mathbf{C}(\Phi \bar{\mathbf{u}})]_{ii} \varphi_i^l \quad (60c)$$

663 where in the second row, the fact that $[\mathbf{C}(\mathbf{u})]_{ij} = 0$ for all $i \neq j$ is used, and in the last row, 664 the fact that $\varphi_i^{k+} = 0$ for all $i \notin \mathcal{V}_k$ is used. Now, considering that $[\mathbf{C}(\mathbf{u})]_{ii}$ has a (1, 1)-th 665 zero element, i.e., $[C_{11}(\Phi \bar{\mathbf{u}})]_{ii} = 0$, and that if $k \neq l$ then $i \notin \mathcal{V}_l$ and thus $\varphi_i^l = \mathbf{0}$, it follows 666 that for some index $i \in \mathcal{V}_k$,

$$\varphi_i^{k+} [\mathbf{C}(\Phi \bar{\mathbf{u}})]_{ii} \varphi_i^l = \varphi_i^{k+} [\mathbf{C}(\Phi \bar{\mathbf{u}})]_{ii} \varphi_i^k = \frac{|E_i|}{|\Omega_k|} [C_{11}(\Phi \bar{\mathbf{u}})]_{ii} = 0 \quad (61)$$

667 The matrix $[\Phi^+ \mathbf{C}(\Phi \bar{\mathbf{u}}) \Phi]_{kl} = 0$ for all $k, l = 1, 2, \dots, N$, and thus,

$$\bar{\mathbf{C}}(\bar{\mathbf{u}}) = \Phi^+ \mathbf{C}(\Phi \bar{\mathbf{u}}) \Phi = \mathbf{0} \quad (62)$$

668 as indicated by the LCM in eq. (11).

669 **A.2.2 Magnitude Analysis for Residual Dynamics**

670 Next, the magnitude of the residual dynamics $\mathbf{r}^{(2)}(\mathbf{u}, t)$ is analyzed to pinpoint the missing
671 physics in the LCM. By definition,

$$\mathbf{r}^{(2)}(\mathbf{u}, t) = \dot{\bar{\mathbf{u}}} - \mathbf{r}^{(1)}(\bar{\mathbf{u}}, t) \quad (63a)$$

$$= \Phi^+ \mathbf{r}(\mathbf{u}, t) - \mathbf{r}^{(1)}(\mathbf{u}, t) \quad (63b)$$

$$= \underbrace{\Phi^+ \mathbf{A}^{-1} \mathbf{B} \mathbf{u} - \bar{\mathbf{A}}(\mathbf{w})^{-1} \bar{\mathbf{B}}(\mathbf{w}) \bar{\mathbf{u}}}_{\#1} + \underbrace{\Phi^+ \mathbf{A}(\mathbf{u})^{-1} \mathbf{C}(\mathbf{u}) \mathbf{u} - \bar{\mathbf{A}}(\mathbf{w})^{-1} \bar{\mathbf{C}}(\bar{\mathbf{u}}) \bar{\mathbf{u}}}_{\#2} \quad (63c)$$

$$+ \underbrace{\Phi^+ \mathbf{A}(\mathbf{u})^{-1} \mathbf{f}(t) - \bar{\mathbf{A}}(\mathbf{w})^{-1} \bar{\mathbf{f}}(t)}_{\#3}$$

672 The magnitude analysis for terms $\#1$ and $\#3$ can be found in Ref. [17]. The analysis for
673 term $\#2$ is presented next. Let $\mathbf{D}(\bar{\mathbf{u}}) = \mathbf{A}(\Phi \bar{\mathbf{u}})^{-1} \mathbf{P} \mathbf{C}(t, \Phi \bar{\mathbf{u}})$, then,

$$\Phi^+ \mathbf{A}(\mathbf{u})^{-1} \mathbf{C}(\mathbf{u}) \mathbf{u} - \bar{\mathbf{A}}(\bar{\mathbf{u}})^{-1} \bar{\mathbf{C}}(t, \bar{\mathbf{u}}) \bar{\mathbf{u}} \quad (64a)$$

$$= \Phi^+ \mathbf{A}(\mathbf{u})^{-1} \mathbf{C}(\mathbf{u}) \mathbf{u} - \Phi^+ \mathbf{A}(\Phi \bar{\mathbf{u}})^{-1} \mathbf{P} \mathbf{C}(t, \Phi \bar{\mathbf{u}}) \Phi \Phi^+ \mathbf{u} \quad (64b)$$

$$= \Phi^+ \mathbf{A}^{-1}(\mathbf{u}) \mathbf{C}(\mathbf{u}) \mathbf{u} - \Phi^+ \mathbf{D}(\bar{\mathbf{u}}) \Phi \Phi^+ \mathbf{u} \quad (64c)$$

$$(64d)$$

674 where $\mathbf{P} = \Phi \Phi^+$. Thus,

$$\|\Phi^+ \mathbf{A}(\mathbf{u})^{-1} \mathbf{C}(\mathbf{u}) \mathbf{u} - \bar{\mathbf{A}}^{-1}(\bar{\mathbf{u}}) \bar{\mathbf{C}}(t, \bar{\mathbf{u}}) \bar{\mathbf{u}}\| \quad (65a)$$

$$\leq \|\Phi^+ \mathbf{A}^{-1}(\mathbf{u}) \mathbf{C}(\mathbf{u}) \mathbf{u} - \Phi^+ \mathbf{D}(\bar{\mathbf{u}}) \mathbf{u}\| + \|\Phi^+ \mathbf{D}(\bar{\mathbf{u}}) \mathbf{u} - \Phi^+ \mathbf{D}(\bar{\mathbf{u}}) \Phi \Phi^+ \mathbf{u}\| \quad (65b)$$

$$\leq \|\Phi^+ \| \underbrace{\|\mathbf{A}^{-1}(\mathbf{u}) \mathbf{C}(\mathbf{u}) \mathbf{u} - \mathbf{D}(\bar{\mathbf{u}}) \mathbf{u}\|}_{\#1} + \|\Phi^+ \mathbf{D}(\bar{\mathbf{u}})\| \underbrace{\|\mathbf{u} - \Phi \Phi^+ \mathbf{u}\|}_{\#2} \quad (65c)$$

675 where term $\#2$ is due to the approximation of non-uniform temperaeture as constants, and
676 term $\#1$ is the error in the advection dynamics due to coarse-graining.

677 **A.3 Lumped Capacitance Model**

678 The following assumptions are employed: (1) the temperature in component (i) is described
679 by a scalar time-varying average temperature $\bar{u}^{(i)}$, (2) between neighboring components (i)
680 and (j) the heat flux is approximated as,

$$q_{ij} = \frac{\bar{u}^{(j)} - \bar{u}^{(i)}}{R_{ij}} \quad (66)$$

681 where R_{ij} is the thermal resistance. Empirically, for a component of isotropic heat conduction
682 with thermal conductivity k , length ℓ , and cross-section area A , the thermal resistance is $R = \ell/kA$. Between
683 components i and j , define $R_{ij} = R_i + R_j$. In addition, the heat flux due to Dirichlet
684 boundary condition is computed as $q_{iT} = (T_b - \bar{u}^{(i)})/R_i$.

685 At component i , the dynamics of LCM are given by,

$$\int_{E^{(i)}} \rho c_p \dot{\bar{u}}^{(i)} dE^{(i)} = \left(\sum_{j \in \mathcal{N}_i} \int_{e_{ij}} \frac{\bar{u}^{(j)} - \bar{u}^{(i)}}{R_{ij}} de_{ij} \right) + \int_{e_{iq}} q_b de_{iq} + \int_{e_{iT}} \frac{T_b - \bar{u}^{(i)}}{R_i} de_{iT} \quad (67a)$$

$$\bar{A}^{(i)} \dot{\bar{u}}^{(i)} = \left(\sum_{j \in \mathcal{N}_i} \frac{|e_{ij}|}{R_{ij}} (\bar{u}^{(j)} - \bar{u}^{(i)}) \right) + |e_{iq}| \bar{q}^{(i)} + \frac{|e_{iT}|}{R_i} (\bar{T}^{(i)} - \bar{u}^{(i)}) \quad (67b)$$

$$= \sum_{j \in \mathcal{N}_i} \left(-\frac{|e_{ij}|}{R_{ij}} \bar{u}^{(i)} + \frac{|e_{ij}|}{R_{ij}} \bar{u}^{(j)} \right) + \left(-\frac{|e_{iT}|}{R_i} \bar{u}^{(i)} \right) + \left(|e_{iq}| \bar{q}^{(i)} + \frac{|e_{iT}|}{R_i} \bar{T}^{(i)} \right) \quad (67c)$$

$$= \sum_{j \in \mathcal{N}_i \cup \{T_b\}} \left(\bar{B}_{ij}^{(i)} \bar{u}^{(i)} + \bar{B}_{ij}^{(j)} \bar{u}^{(j)} \right) + \bar{f}^{(i)} \quad (67d)$$

686 where in eq. (67b) $|e|$ denotes the length ($d = 2$) or area ($d = 3$) of a component boundary
687 e . The $\bar{A}^{(i)}$, $\bar{B}_{ij}^{(i)}$, and $\bar{B}_{ij}^{(j)}$ quantities are provided in eq. (14).

688 The lumped-mass representation for the four-component TPS is shown in Fig. ???. Let
689 v_i represent the area of the i -th element, $\overline{\rho c_p}_i$, the heat capacity evaluated using the average
690 temperature $\bar{u}^{(i)}$, and $1/R_{ij} = 1/R_i(\bar{u}^{(i)}) + 1/R_j(\bar{u}^{(j)})$ the equivalent thermal resistance
691 between elements i and j . Leveraging the formulas from eqs. (13) and (14), the LCM
692 matrices are given by,

$$\bar{\mathbf{A}} = \begin{bmatrix} \overline{\rho c_p}_1 v_1 & 0 & 0 & 0 \\ 0 & \overline{\rho c_p}_2 v_2 & 0 & 0 \\ 0 & 0 & \overline{\rho c_p}_3 v_3 & 0 \\ 0 & 0 & 0 & \overline{\rho c_p}_4 v_4 \end{bmatrix}, \quad (68a)$$

$$\bar{\mathbf{B}} = \begin{bmatrix} \frac{1}{R_{12}} + \frac{1}{R_{14}} & -\frac{1}{R_{12}} & 0 & -\frac{1}{R_{14}} \\ -\frac{1}{R_{12}} & \frac{1}{R_{12}} + \frac{1}{R_{24}} + \frac{1}{R_{23}} & -\frac{1}{R_{23}} & -\frac{1}{R_{24}} \\ 0 & -\frac{1}{R_{32}} & \frac{1}{R_{32}} + \frac{1}{R_{34}} & -\frac{1}{R_{34}} \\ -\frac{1}{R_{14}} & -\frac{1}{R_{24}} & -\frac{1}{R_{34}} & \frac{1}{R_{14}} + \frac{1}{R_{24}} + \frac{1}{R_{34}} \end{bmatrix}, \quad \bar{\mathbf{f}} = \begin{bmatrix} \bar{q}^{(1)} \\ \bar{q}^{(2)} \\ \bar{q}^{(3)} \\ 0 \end{bmatrix} \quad (68b)$$

693 References

- [1] Adam J. Amar, A. Brandon Oliver, Benjamin S. Kirk, Giovanni Salazar, and Justin Drob. Overview of the charring ablator response (char) code. In AIAA, editor, *AIAA Aviation Forum*, 2016.
- [2] Guy L. Bergel, Frank B. Beckwith, Gabel J. de Frias, Kevin M. Manktelow, Mark T. Merewether, Scott T. Miller, Krishen J. Parmar, Timothy S. Shelton, Jesse T. Thomas, Jeremy T. Trageser, Benjamin T. Treweek, Michael V. Veilleux, and Ellen B. Wagman. *Sierra/SolidMechanics 5.6 User's Manual*, 2022.
- [3] Ricky T. Q. Chen, Yulia Rubanova, Jesse Bettencourt, and David Duvenaud. Neural ordinary differential equations, 2019.

- [4] Jonathan Clausen, Victor Brunini, Lincoln Collins, Robert C Knaus, Alec Kucala, Stephen Lin, Daniel Robert Moser, Malachi Phillips, Thomas Michael Ransegrenola, Samuel Ramirez Subia, et al. Sierra multimechanics module: Aria verification manual-version 5.22. Technical report, Sandia National Lab.(SNL-NM), Albuquerque, NM (United States), 2024.
- [5] Gary Cohen and Sebastien Pernet. *Finite Element and Discontinuous Galerkin Methods for Transient Wave Equations*. Springer Dordrecht, Le Chesnay and Toulouse France, 2018.
- [6] Jianhao Fang, Weifei Hu, Zhenyu Liu, Yuhao Zhou, Chao Wei, and Jianrong Tan. A reduced order finite element-informed surrogate model for approximating global high-fidelity simulations. *Structural and Multidisciplinary Optimization*, 67(12), 2024.
- [7] Matthew Gasch, Keith Peterson, Mairead Stackpoole, Ethiraj Venkatapathy, Gregory Gonzales, and Kyle Hendrickson. Development of advanced ablative carbon phenolic tps for future nasa missions and commercial space. In *38th Annual Small Satellite Conference*, Logan, Utah, May 2024.
- [8] Micah A. Howard and Ben F. Blackwell. A multi-dimensional finite element based solver for decomposing and non-decomposing thermal protection systems. In AIAA, editor, *AIAA Aviation Forum*, 2015.
- [9] Frank P. Incropera, David P. DeWitt, Theodore L. Bergman, and Adrienne S. Lavine. *Fundamentals of Heat and Mass Transfer*. Wiley, Hoboken, NJ, 7th edition, 2011.
- [10] R. J. Klock and Carlos Cesnik. Nonlinear thermal reduced-order modeling for hypersonic vehicles. *AIAA Journal*, 55(7), 2017.
- [11] Arun Govind Neelan. Linear and non-linear reduced order model of scramjet. In *Advances in Multidisciplinary Design, Analysis and Optimization*, pages 111–118, Singapore, 2025.
- [12] Alberto Padovan, Blaine Vollmer, Francesco Panerai, Marco Panesi, Kelly A. Stephani, and Daniel J. Bodony. An extended bformulation for ablating-surface boundary conditions. *International Journal of Heat and Mass Transfer*, 218:124770, 2024.
- [13] Eric Parish and Karthik Duraisamy. Non-markovian closure models for large eddy simulations using the mori-zwanzig formalism. *Phys. Rev. Fluids*, 2:014604, Jan 2017.
- [14] Eric Parish and Karthik Duraisamy. A unified framework for multiscale modeling using the mori-zwanzig formalism and the variational multiscale method. *ArXiv*, 12 2017.
- [15] Eric Parish and Karthik Duraisamy. *Coarse-Graining Turbulence Using the Mori-Zwanzig Formalism*. Cambridge University Press, Cambridge, 2025.
- [16] Adam Thelen, Xiaoge Zhang, Olga Fink, Yan Lu, Sayan Ghosh, Byeng D. Youn, Michael D. Todd, Sankaran Mahadean, Chao Hu, and Zhen Hu. A comprehensive review of digital twin – part 1: modeling and twinning enabling technologies. *Structural and Multidisciplinary Optimization*, 65(12), 2022.

- ⁷⁴¹ [17] Carlos A. Vargas Venegas, Daning Huang, Patrick Blonigan, and John Tencer. Physics-
⁷⁴² infused reduced-order modeling for analysis of multi-layered hypersonic thermal protec-
⁷⁴³ tion systems, 2025.
- ⁷⁴⁴ [18] Yongyong Xian, Baisong Pan, and Luping Luo. A new model updating strategy with
⁷⁴⁵ physics-based and data-driven models. *Structural and Multidisciplinary Optimization*,
⁷⁴⁶ 64(1), 2021.
- ⁷⁴⁷ [19] Yin Yu, John Harlim, Daning Huang, and Yan Li. Learning coarse-grained dynamics
⁷⁴⁸ on graph. *arXiv preprint arXiv:2405.09324*, 2024.